

Perez et al. Resubmission

1 **A novel, ataxic mouse model of Ataxia Telangiectasia caused by a**
2 **clinically relevant nonsense mutation**

3 Perez, Harvey ^{‡1}; Abdallah, May, F. ^{‡1}; Chavira, Jose, I. ^{‡1}; Egeland, Martin, T. ¹; Vo, Karen, L. ¹;
4 Buechsenschuetz, Callan, L. ¹; Sanghez, Valentina ¹; Kim, Jeannie, L. ¹; Pind, Molly ², Nakamura,
5 Kotoka ³, Hicks, Geoffrey, G. ²; Gatti, Richard, A. ³; Madrenas, Joaquin ^{1,5}; Iacovino, Michelina ^{1,4};
6 McKinnon, Peter, J. ⁶; Mathews, Paul, J. ^{*1,7}

7 1. *The Lundquist Institute for Biomedical Innovation, Harbor-UCLA Medical Center, Torrance, CA*
8 2. *Department of Biochemistry & Medical Genetics, Max Rady College of Medicine, University of*
9 *Manitoba*
10 3. *Department of Pathology & Laboratory Medicine, David Geffen School of Medicine, University of*
11 *California, Los Angeles, CA*
12 4. *Department of Pediatrics, Harbor-UCLA Medical Center, Torrance, CA*
13 5. *Department of Medicine, Harbor-UCLA Medical Center, Torrance, CA*
14 6. *Center for Pediatric Neurological Disease Research, St. Jude Translational Neuroscience, St.*
15 *Jude Children's Research Hospital, Memphis, TN, USA*
16 7. *Department of Neurology, Harbor-UCLA Medical Center, Torrance, CA*

17 [‡]*Contributed equally*

18 ^{*}*Corresponding Author*

19 **Abstract**

20 Ataxia Telangiectasia (A-T) and ataxia with ocular apraxia type 1 (AOA1) are devastating neurological
21 disorders caused by null mutations in the genome stability genes, A-T mutated (*ATM*) and aprataxin
22 (*APTX*), respectively. Our mechanistic understanding and therapeutic repertoire for treating these
23 disorders is severely lacking, in large part due to the failure of prior animal models with similar null
24 mutations recapitulating the characteristic loss of motor coordination (i.e., ataxia) and associated
25 cerebellar defects. By increasing genotoxic stress, through the insertion of null mutations in both the
26 *Atm* (nonsense) and *Aptx* (knockout) genes in the same animal, we have generated a novel mouse
27 model that for the first time progressively develops a severe ataxic phenotype associated with atrophy
28 of the cerebellar molecular layer. We find biophysical properties of cerebellar Purkinje neurons are
29 significantly perturbed (e.g., reduced membrane capacitance, lower action potential thresholds, etc.),
30 while properties of synaptic inputs remain largely unchanged. These perturbations significantly alter

Perez et al. Resubmission

31 Purkinje neuron neural activity, including a progressive reduction in spontaneous action potential firing
32 frequency that correlates with both cerebellar atrophy and ataxia over the animal's first year of life.
33 Double mutant mice also exhibit a high predisposition to developing cancer (thymomas) and immune
34 abnormalities (impaired early thymocyte development and T-cell maturation), symptoms characteristic
35 of the disorder A-T. Lastly, by inserting a clinically relevant nonsense type null mutation in *Atm*, we
36 demonstrate that small molecule readthrough (SMRT) compounds can restore ATM production,
37 indicating their potential as a future A-T therapeutic.

38 1.0 Introduction

39 Ataxia Telangiectasia (A-T) is a rare (1 in ~100,000) (Swift et al. 1986), autosomal recessive genetic
40 disorder characterized by cancer predisposition, immune deficiency, and a highly penetrant progressive
41 and severe ataxia linked to cerebellar atrophy (Rothblum-Oviatt et al. 2016; Boder and Sedgwick 1958;
42 Levy and Lang 2018). A-T patients typically die in their second and third decade of life (Crawford et al.
43 2006) from lymphatic cancers, respiratory infections, or debilitating ataxia—unfortunately, survivability
44 has not dramatically changed since the 1950s (Micol et al. 2011; Rothblum-Oviatt et al. 2016). While
45 disease progression and cause of death vary widely across patients, the highly penetrant progressive
46 decline in motor coordination is reported as having the greatest negative impact on a patient's quality of
47 life (Jackson et al. 2016). Care is generally palliative, directed at reducing, limiting, or eliminating
48 cancers or infections. No long-term therapies are available for treating the ataxia and associated
49 cerebellar dysfunction and atrophy.

50 A-T is caused by deficiency or dysfunction of the ATM (A-T mutated) protein (Savitsky et al. 1995).
51 Premature termination codon (PTC) causing nonsense mutations account for up to a half of known
52 cases with missense and deletions also contributing (Concannon and Gatti 1997; Sandoval et al. 1999).
53 ATM is a serine/threonine PIKK family kinase that plays a key role in the DNA damage response
54 (DDR), protecting cells from the tens of thousands of DNA lesions incurred each day (Lindahl and
55 Barnes 2000; Kastan and Bartek 2004; Shiloh and Ziv 2013). In the active monomeric form, ATM
56 phosphorylates several key proteins halting the production of new DNA (cell cycle arrest) (Ando et al.

Perez et al. Resubmission

57 2012), and then, depending on severity of the damage, initiating DNA repair or programmed cell death
58 (i.e., apoptosis) (Ando et al. 2012; Rashi-Elkeles et al. 2006). Several downstream DDR pathway
59 targets of ATM have been identified, including p53, CHK2, BRCA1, SMC1, and NBS1 (Matsuoka et al.
60 2007). ATM's role in DNA repair is also implicated in normal immune system development, where it is
61 proposed to contribute to the recombination of natural DNA splicing that occurs during gene
62 rearrangement in T- and B-lymphocyte maturation (Chao, Yang, and Xu 2000; Matei, Guidos, and
63 Danska 2006; Vacchio et al. 2007; Schubert, Reichenbach, and Zielen 2002). Although its roles are still
64 emerging, ATM has also been implicated in oxidative stress homeostasis (Guo et al. 2010) and
65 mitophagy (Valentin-Vega and Kastan 2012; Pizzamiglio, Focchi, and Antonucci 2020).

66 A mechanistic understanding of why ATM deficiency causes ataxia is still under debate, but it is far
67 from the only DDR protein linked to ataxia, as aprataxin (APTX) (Aicardi et al. 1988), meiotic
68 recombination 11 homolog 1 (MRE11) (Sedghi et al. 2018), nibrin (NBS1) (van der Burgt et al. 1996),
69 senataxin (SETX) (Moreira et al. 2004), and tyrosyl-DNA phosphodiesterase 1 (TDP1) (Takashima et
70 al. 2002) when absent or dysfunctional can cause cerebellar-related ataxia. This suggests that the
71 neurological features of genome instability syndromes have a common underlying cause, although this
72 idea is still to be mechanistically demonstrated (McKinnon 2009; Rass, Ahel, and West 2007).

73 A major factor limiting our ability to define why loss of DDR proteins, like ATM, selectively impacts the
74 cerebellum and causes progressive ataxia is the lack of an animal model that recapitulates these
75 neurological symptoms (Lavin 2013). Several A-T rodent models have been created over the past
76 several years by inserting gene mutations that cause protein dysfunction (lack kinase activity) or
77 complete deficiency (Herzog et al. 1998; Xu and Baltimore 1996; Elson et al. 1996; Spring et al. 2001;
78 Campbell et al. 2015; Quek et al. 2016; Tal et al. 2018; Lavin 2013); a minipig was also recently
79 reported (Beraldi et al. 2017). Unfortunately, none acquire an overt, progressive ataxia with cerebellar
80 dysfunction and atrophy that recapitulates the human disease, even though other aspects of the
81 disorder like thyroid cancers, infertility, and immune abnormalities do develop. It remains unclear why
82 these prior animal models fail to display the progressive ataxic phenotype (Lavin 2013). It is possible

Perez et al. Resubmission

83 that species specific molecular compensations in mice provide redundancies or alternative pathways
84 minimizing the effects of ATM deficiency in the brain (El-Brolosy and Stainier 2017). It is also possible
85 that the shortened lifespan of prior models (Barlow et al. 1996) is too brief for the stochastic
86 mechanisms driving cerebellar dysfunction and atrophy to accumulate and impact motor behavior.
87 Other challenges include potentially leaky genetic manipulations that result in low levels of ATM protein
88 or active fragments with residual kinase activity, thus limiting neuropathology (Li et al. 2011). The
89 impact of missing such a crucial animal model has been significant, severely limiting not only
90 experimental studies from identifying the cellular and molecular mechanisms but hampering pre-clinical
91 development and testing of much needed therapeutics.

92 We test here whether increasing genotoxic stress, by placing null mutations in not just the *Atm* gene,
93 but also the related *Aptx* gene, leads to a more representative mouse model that displays cerebellar
94 dysfunction, atrophy, and the development of progressive ataxia. We chose to additionally knock-out
95 *Aptx* because its deficiency causes an A-T like disorder in humans called ataxia with ocular apraxia
96 type 1 (AOA1), but without A-T's other system defects that could increase the potential for prenatal
97 lethality or early death (e.g., immunodeficiency and cancer predisposition) (Coutinho P 2002).
98 Moreover, APTX is a phosphodiesterase involved in DNA reassembly after double and single stranded
99 repair, having a function downstream of, but not directly regulated or related to ATM (Gueven et al.
100 2004; Schellenberg, Tumbale, and Williams 2015; Ahel et al. 2006). We therefore reasoned that
101 deficiency of both proteins would have an additive effect on genotoxic stress capable of inducing a
102 detectable neurological dysfunction. Our results indeed demonstrate that mice deficient in ATM and
103 APTX develop cerebellar dysfunction, atrophy, and a progressive and profound ataxia, while deficiency
104 in either protein alone do not. Additionally, double mutants acquired several additional characteristic
105 symptoms of A-T, including defects in immune maturation and a high incidence of cancer (thymomas),
106 making it the most representative model, from a phenotypic standpoint, to date.

107 Finally, to improve the clinical and translational relevance of this new mouse model, we inserted a point
108 mutation (103C>T) in the *Atm* gene common to a large family North African A-T patients. This mutation

Perez et al. Resubmission

109 results in a premature termination codon (PTC) at what would normally be amino acid 35 resulting in
110 loss of ATM production. As a result of this genotypic mutation, we were then able to conduct proof-of-
111 principle experiments demonstrating the ability of so-called PTC readthrough therapeutics to restore
112 production of the ATM protein. This includes the Small Molecule Readthrough (SMRT) compound,
113 GJ103 we are currently developing (Du et al. 2013).

114 2.0 Results

115 2.1 Creation of a new A-T mutant mouse model expressing a clinically relevant nonsense 116 mutation

117 To create a more clinically relevant mouse model of A-T we used a gateway recombination cloning and
118 site-directed mutagenesis method to recapitulate a c.103C>T (p.R35X) mutation in the *ATM* gene
119 found in a large population of North African A-T patients (**Fig. 1A and Methods**) (Gilad et al. 1996).
120 The insertion of thymine in place of cytosine at this site in exon 3 results in a premature termination
121 codon (PTC) causing nonsense mutation in the ATM gene. Since the c.103C>T mutation results in
122 different PTCs in the human compared to the mouse *Atm* gene, TGA vs. TAG respectively, we created
123 two different mice by exchanging the mouse *Atm* exon 3 with either a human or mouse exon 3 variant
124 with the c.103C>T mutation (**Fig. 1B**). In the human variant, a 103C>T mutation of the mouse codon,
125 where the arginine (R) encoding codon (CGA) becomes a TGA stop codon, results in a mouse we
126 denote as *Atm*^{R35X} (officially *Atm*^{Tm1.1(103CAG)TGA)Mfgc}). In the mouse variant, the c.103C>T mutation
127 transforms a glutamine (Q) encoding CAG codon into a TAG stop codon and is denoted *Atm*^{Q35X}
128 (officially *Atm*^{Tm1.1(103C)T)Mfgc}). The presence of the PTC results in a loss of ATM expression, either
129 reduced by about half in the heterozygote expressing one normal mouse copy of the *Atm* gene
130 (*Atm*^{R35X/+} or *Atm*^{Q35X/+}), or completely in the homozygote (*Atm*^{R35X/R35X} or *Atm*^{Q35X/Q35X}) (**Fig. 1C**).

131 *Atm*^{R35X/R35X}; *Aptx*^{-/-} mice were created by first crossing single mutant *Atm*^{R35X/R35X} (congenic on the
132 C57BL/6J background) and *Aptx*^{-/-} (mixed C57BL/6J and 129 background) mice to generate double
133 mutant heterozygote *Atm*^{R35X/+}; *Aptx*^{+/-} mice. F1-5 littermate *Atm*^{R35X/+}; *Aptx*^{+/-} mice were then crossed
134 within litters to create sufficient numbers of the desired experimental and control genotypes to

Perez et al. Resubmission

135 determine how loss of different amounts of ATM and APTX affect the animal's phenotype (**Fig. 1D**).
136 Like prior ATM deficient A-T mouse models, ATM or APTX deficiency alone did not result in mice with
137 ataxia (**Video 1 and 2**). However, deficiency in both proteins ($Atm^{R35X/R35X}; Aptx^{-/-}$) results in the
138 development of a severe and progressively ataxic phenotype (**Fig. 1E, Video 3 and 4**).

139 **2.2 ATM deficient mice have lowered survivability and a high incidence of thymomas**

140 We assessed the general health and development of control and experimental mice expressing
141 different levels of ATM and APTX (**Fig. 2**). We found that $Atm^{R35X/R35X}; Aptx^{-/-}$ mice grew ~55% slower
142 and reached estimated plateau weights that were ~35% less than control genotypes (log-rank, $n = 21$ to
143 40, $p < 0.0001$; **Fig. 2A**). These differences in weight were a postnatal phenomenon, as no significant
144 weight differences were detected just after birth (P8) across all genotypes (1-way ANOVA, $n = 5$ to 23,
145 $p > 0.23$). Adolescent double mutant mice at postnatal day 45 (P45) weighed on average 30% less in
146 males double mutant: 14.4 ± 1.0 g ($n = 13$) vs. wildtype: 20.2 ± 0.5 g ($n = 16$), t -test, $p < 0.0001$] and 25%
147 less in females [double mutant: 12.7 ± 0.6 g ($n = 17$) vs. wildtype: 17.0 ± 0.2 g ($n = 15$), t -test, $p < 0.0001$;
148 **Fig. 1A**]. Differences across the control genotypes were observed, but they were small and not
149 consistent across time points or sex and therefore judged to not be physiologically relevant (**Fig. 2A**).
150 Survivability of the $Atm^{R35X/R35X}; Aptx^{-/-}$ mice was significantly reduced compared to $Atm^{+/+}; Aptx^{+/+}$ mice,
151 with 53% of mice still alive at 400 days of age, compared to 97% of $Atm^{+/+}; Aptx^{+/+}$ mice at the same
152 time point (**Fig. 2B**). ATM deficiency alone was sufficient to reduce survivability, as compared to $Atm^{+/+};$
153 $Aptx^{+/+}$ mice, both $Atm^{R35X/R35X}; Aptx^{+/+}$ and $Atm^{R35X/R35X}; Aptx^{-/-}$ mice had significantly reduced
154 survivability rates [42%, log-rank, $\chi^2_{(1, 56)} = 13.49$, $p = 0.0002$ and 52%, log-rank, $\chi^2_{(1, 53)} = 19.54$, $p < 0.0001$,
155 respectively]. No significant difference between ATM deficient mice with partial or complete APTX
156 deficiency was detected [log-rank, $\chi^2_{(2, 85)} = 1.01$, $p = 0.6$]. Conversely, mice harboring at least one
157 functional copy of the *Atm* gene had normal survivability rates, regardless of whether they expressed
158 APTX or not [log-rank, $\chi^2_{(3, 131)} = 3.08$, $p = 0.4$]. No significant difference between male and female mice
159 was observed and thus data were pooled [log-rank, $p > 0.4$ for all pairwise comparisons; **Fig. 2-fig. S1B**].
160 Generally, a third of mice with ATM deficiency died from complications related to large thymic cancers

Perez et al. Resubmission

161 (thymoma) found in the thoracic cavity (**Fig. 2C**). The presence or absence of APTX did not impact
162 cancer prevalence, and mice with at least one *Atm* transcript were cancer free up until at least P400.
163 Overall, ATM, but not APTX deficiency had severe effects on the health and survivability of mice.

164 **2.3 Both ATM and APTX deficiency are necessary to produce progressive motor dysfunction**

165 The progressive development of severe ataxia is a hallmark characteristic of A-T that is recapitulated in
166 the *Atm*^{R35X/R35X}; *Aptx*^{-/-} mice but none of the other control genotypes we tested. Overall, we find motor
167 coordination deficits emerge between 210 and 400 days after birth in *Atm*^{R35X/R35X}; *Aptx*^{-/-} mice and find
168 no evidence of ataxia in mice with at least one copy of the *Atm* or *Aptx* gene (**Fig. 3A, B**). For the
169 vertical pole test, *Atm*^{R35X/R35X}; *Aptx*^{-/-} mice took twice as long to descend at P400 compared to *Atm*^{+/+};
170 *Aptx*^{+/+}, *Atm*^{+/+}; *Aptx*^{-/-}, *Atm*^{R35X/R35X}; *Aptx*^{+/+}, or *Atm*^{R35X/+}; *Aptx*^{-/-} mice [Male: 29.1 ± 0.9 s (n = 3) vs. 7.5 ±
171 0.4 s (n = 12), 12.5 ± 2.5 s (n = 9), 9.2 ± 0.9 s (n = 10), 8.6 ± 0.9 s (n = 11), 1-way ANOVA, $F_{(4, 40)} = 19.9$,
172 $p < 0.0001$; Female: 19.0 ± 4.0 s (n = 4) vs. 7.5 ± 0.4 s (n = 12), 7.8 ± 0.4 s (n = 10), 10.5 ± 1.2 s (n = 6),
173 8.2 ± 0.5 s (n = 8), 1-way ANOVA, $F_{(4, 35)} = 13.9$, $p < 0.0001$]. An examination of gait indicated that
174 *Atm*^{R35X/R35X}; *Aptx*^{-/-} mice at P400, but not P210 need additional stabilization during ambulation, as they
175 spend twice as much time with 3 paws, rather than the normal 2 in contact with the ground as they walk
176 across the gait analysis platform [Male: 56.2 vs. 26.4 to 32.2 %, 1-way ANOVA, $F_{(4, 54)} = 14.3$, $p < 0.0001$;
177 Female: 58.4 vs. 18.9 to 28.8 %, 1-way ANOVA, $F_{(3, 178)} = 95.5$, $p < 0.0001$; **Fig. 3B**]. *Atm*^{R35X/R35X}; *Aptx*^{-/-}
178 also display a slower cadence and average speed across the platform compared to all other genotypes
179 at P400 [cadence, Male: 9.5 vs. 13.3 to 15.9 steps/s, 1-way ANOVA, $F_{(3, 204)} = 36.8$, $p < 0.0001$; Female:
180 9.1 vs. 14.2 to 15.9 steps/s, 1-way ANOVA, $F_{(3, 204)} = 39.7$, $p < 0.0001$; speed, Male: 8.8 vs. 22 to 26 cm/s,
181 1-way ANOVA, $F_{(4, 50)} = 28.3$, $p < 0.0001$; Female: 58.4 vs. 18.9 to 28.8 cm/s, 1-way ANOVA, $F_{(3, 178)} =$
182 39.7, $p < 0.0001$; **Fig. 3B**; **Fig. 3-fig. S1**]. This difference in speed and cadence is unlikely due to animal
183 size, as there are no significant differences in these parameters at earlier time points when the
184 difference in size is significant (**Fig. 2A**). These observations across the two behavioral tests were
185 found in both male and female mice at each of their respective time points, consistent with the lack of
186 sex differences observed in A-T patients.

Perez et al. Resubmission

187 We further examined behavioral differences between the $Atm^{R35X/R35X}$, $Aptx^{-/-}$ and $Atm^{+/+}$; $Aptx^{+/+}$ mice
188 using a standardized set of experimental procedures used to phenotype genetically modified mice (i.e.,
189 SHIRPA; **Fig. 3C**; **Fig. 3-fig. S1**) (Rogers et al. 1997). We first detected differences in motor function at
190 P8, where $Atm^{R35X/R35X}$; $Aptx^{-/-}$ mice took 3-4 times longer on average to right themselves compared to
191 $Atm^{+/+}$; $Aptx^{+/+}$ mice [Male: 6.4 ± 1.1 s (n = 24) vs. 1.5 ± 0.1 s (n = 23), *t*-test, $p < 0.0002$; Female: $11.1 \pm$
192 1.9 s (n = 21) vs. 2.4 ± 0.3 s (n = 17), *t*-test, $p < 0.0002$; **Fig. 3C bottom**]. At 30-days of age, we detected
193 significant differences between $Atm^{R35X/R35X}$; $Aptx^{-/-}$ and $Atm^{+/+}$; $Aptx^{+/+}$ mice in behavioral tests that
194 qualitatively measure body position and spontaneous activity (**Fig. 3C**). Striking differences in
195 $Atm^{R35X/R35X}$; $Aptx^{-/-}$ compared to $Atm^{+/+}$; $Aptx^{+/+}$ mice were observed at P400, especially for behaviors
196 related to movement, including locomotor activity, body position, and gait (**Fig. 3C**). The results from
197 this battery of tests demonstrates that $Atm^{R35X/R35X}$; $Aptx^{-/-}$ mice develop a severe change in behavior by
198 P400, consistent with purely visual observations of significant motor coordination deficits in the mice up
199 to this time point. Importantly, we do not find any significant differences between the other control
200 genotypes, including $Atm^{R35X/+}$; $Aptx^{-/-}$ mice that express at least some ATM but no APTX protein (**Fig.**
201 **3-fig. S1**).

202 **2.4 The membrane and synaptic properties are perturbed in ATM and APTX deficient neurons of** 203 **the cerebellum**

204 Purkinje neurons (PN) are a key neuronal subtype located in the cerebellar cortex. They display
205 considerable intrinsic excitability, firing action potentials spontaneously at rates significantly higher than
206 most other neurons in the brain (50 to 100 Hz more in many cases). Their activity shapes cerebellar
207 output via tonic inhibition of neurons of the cerebellar nuclei, which project to motor coordination
208 centers in the forebrain, brainstem, and spinal cord. Dysfunction of cerebellar PNs is associated with
209 several forms of ataxia and implicated in A-T (Hoxha et al. 2018; Cook, Fields, and Watt 2020; Shiloh
210 2020). We therefore examined if the electrophysiological properties of PNs in the $Atm^{R35X/R35X}$; $Aptx^{-/-}$
211 cerebellum were abnormal.

Perez et al. Resubmission

212 Since PN baseline activity and responsivity to input is mediated by a baseline set of passive and active
213 membrane properties (**Fig. 4**), we directly recorded from and compared the membrane properties of
214 PNs in acute cerebellar slices harvested from *Atm*^{R35X/R35X}; *Aptx*^{-/-} and *Atm*^{+/+}; *Aptx*^{+/+} mice (P350 to
215 400). PNs recorded from *Atm*^{R35X/R35X}; *Aptx*^{-/-} mice had significantly “tighter” membranes, displaying
216 higher membrane input resistances (R_m) than those from *Atm*^{+/+}; *Aptx*^{+/+} mice [47.7 ± 5.6 (n = 15) vs.
217 30.2 ± 1.47 (n = 23) M Ω , *t*-test, *p*=0.008; **Fig. 4B**]. They also displayed a faster membrane time
218 constant (τ) [3.6 ± 0.4 (n = 15) vs. 5.1 ± 0.3 (n = 23) ms, *t*-test, *p*=0.009; **Fig. 4B**]. These results indicate
219 that the total membrane capacitance ($C_m = \tau/R_m$) of the *Atm*^{R35X/R35X}; *Aptx*^{-/-} PNs is significantly reduced
220 [98.25 ± 19.23 (n = 15) vs. 175.6 ± 12.67 (n = 23) pF, *t*-test, *p*=0.0025; **Fig. 4B**]. At the cellular level, this
221 suggests that the ATM and APTX deficient PNs have less (i.e., smaller in size) or thinner membranes
222 than that of wildtype PNs; a result suggestive of a developmental deficit or neurodegenerative process
223 (Dell’Orco et al. 2015). We next assessed the intrinsic excitability of PNs in *Atm*^{R35X/R35X}; *Aptx*^{-/-} and
224 *Atm*^{+/+}; *Aptx*^{+/+} mice by examining PN action potential (AP) generation and dynamics. Significant deficits
225 in the ability of PNs to fire continuously in response to current injection were observed in *Atm*^{R35X/R35X};
226 *Aptx*^{-/-} mice (**Fig. 4C**). These deficits were associated with significant perturbations to the amplitude,
227 threshold, and area of evoked action potentials [amplitude: 66.2 ± 0.7 (n = 14) vs. 72.1 ± 1.4 (n = 13)
228 Δ mV, *t*-test, *p* = 0.003; threshold: -55.2 ± 1.5 vs. -48.61 ± 1.9 mV, *t*-test, *p*=0.0196; area: 17.96 ± 0.6 vs.
229 20.63 ± 1.0 mV*ms, *t*-test, *p*=0.048; **Fig. 4C**]. Together, these experiments demonstrate significant
230 perturbations of PN physiological properties that likely perturb their ability to function normally in the
231 cerebellum of *Atm*^{R35X/R35X}; *Aptx*^{-/-} mice.

232 We next tested whether extrinsic and/or synaptic PN properties were also impacted in *Atm*^{R35X/R35X};
233 *Aptx*^{-/-} mice. We first examined spontaneous mini excitatory post synaptic currents (mEPSC) generated
234 by granule cell-to-PN synapses (i.e., parallel fiber inputs). No difference in mEPSC size was detected,
235 indicating the function of granule cell axon terminals (i.e. parallel fibers) was relatively normal in the
236 *Atm*^{R35X/R35X}; *Aptx*^{-/-} cerebellum [18.92 ± 1.3 (n = 11) vs. 23.4 ± 3.3 (n = 11) pA, *t*-test, *p*=0.477; **Fig. 4D**]
237 (Yamasaki, Hashimoto, and Kano 2006). mEPSC frequency however, was found to be significantly

Perez et al. Resubmission

238 increased, a phenomenon that could be attributed to either an increase in the total number of synapses,
239 an increase in the size of the readily releasable pool of synaptic vesicles, or an increase in the
240 probability of neurotransmitter release in PNs of *Atm*^{R35X/R35X}; *Aptx*^{-/-} mice [18.75 ± 2.8 Hz (n = 11) vs.
241 11.4 ± 1.0 Hz (n = 11), *t*-test, *p*=0.047; **Fig. 4D**]. We next explored evoked synaptic release and short-
242 term plasticity by simultaneously recording from PNs and electrically stimulating either granule cell (i.e.,
243 parallel fibers) or inferior olivary (i.e., climbing fiber) axons with a paired-pulse burst (2-pulses, 50 ms
244 apart). The synaptic properties of parallel fibers were found to be normal, displaying no significant
245 differences in the expected short-term facilitation (Atluri and Regehr 1996) or halfwidth and decay time
246 constant of the evoked EPSC [PPR: 1.3 ± 0.03 (n = 10) vs. 1.4 ± 0.05 (n = 13), *t*-test, *p*=0.162; halfwidth:
247 3.9 ± 0.6 vs. 4.9 ± 0.4 ms, *t*-test, *p*=0.175; time constant: 3.5 ± 0.5 vs. 4.7 ± 0.4 ms, *t*-test, *p*=0.054; **Fig.**
248 **4E**]. In comparison, we found climbing fiber-to-PN synaptic responses, which normally displays pair-
249 pulse depression (Hansel and Linden 2000), to depress at significantly greater magnitudes in
250 *Atm*^{R35X/R35X}; *Aptx*^{-/-} mice [PPR: 0.6 ± 0.03 (n = 6) vs. 0.7 ± 0.02 (n = 9), *t*-test, *p*=0.03; **Fig. 4F**]. The
251 overall width and decay time constant of the evoked currents were also smaller [halfwidth: 2.3 ± 0.6 (n =
252 6) vs. 3.0 ± 0.2 (n = 9) ms, *t*-test, *p*=0.004; time constant (fast): 1.1 ± 0.14 vs. 2.9 ± 0.4 ms, *t*-test,
253 *p*=0.001]. While these results could be caused by a presynaptic deficit, such as reduced vesicle stores
254 in the climbing fiber axon terminal, the fact that the initial magnitude of the EPSC is unaffected [$23.5 \pm$
255 3.6 (n = 6) vs. 19.1 ± 1.9 (n = 9), *t*-test, *p*=0.3], points to a more intrinsic deficit, such as a reduced Ca²⁺
256 influx from the endoplasmic reticulum, which could significantly impact long term synaptic plasticity
257 critical to cerebellar function (Hoxha et al. 2018; Kano and Watanabe 2017). Overall, the perturbations
258 we observed here to the passive and active PN properties likely give rise to significant cerebellar
259 dysfunction in the *Atm*^{R35X/R35X}; *Aptx*^{-/-} mice.

260 **2.5 ATM and APTX deficiency causes a progressive perturbation of PN neural activity that is** 261 **associated with dendritic shrinking and overall cerebellar atrophy.**

262 Decreased rates of spontaneous PN action potential firing, which can be indicative of PN dysfunction,
263 have been observed in several mouse models of ataxia, including spinocerebellar ataxia (SCA) 2, 3, 5,

Perez et al. Resubmission

264 6, 13, 27, several models of episodic ataxia (e.g., leaner, ducky, and tottering), and autosomal-
265 recessive spastic ataxia of the Charlevoix-Saguenay ((Hourez et al. 2011; Hansen et al. 2013;
266 Dell'Orco, Pulst, and Shakkottai 2017; Kasumu and Bezprozvanny 2012; Liu et al. 2009; Perkins et al.
267 2010; Shakkottai et al. 2011a; Jayabal et al. 2016; Stoyas et al. 2020; Hurlock, McMahon, and Joho
268 2008; Shakkottai et al. 2009; Bosch et al. 2015; Walter et al. 2006; Alviña and Khodakhah 2010; Ady et
269 al. 2018; Larivière et al. 2019; Cook, Fields, and Watt 2020). We therefore used this biomarker to
270 characterize the progression of PN perturbation in *Atm*^{R35X/R35X}; *Aptx*^{-/-} mice and assess whether deficits
271 were restricted to ATM and APTX deficient mice, consistent with the behavioral results (**Fig. 2,3**). We
272 additionally examined whether decreased PN activity differed across the cerebellum, as anecdotal
273 clinical pathology reports suggest degeneration may occur asymmetrically across the cerebellum, with
274 the anterior and posterior vermis and middle cerebellar hemispheres affected the most, although no
275 systematic analysis has been performed and the consistency of results across patients is highly
276 variable (Verhagen et al. 2012; De Leon, Grover, and Huff 1976; Amromin, Boder, and Teplitz 1979;
277 Monaco et al. 1988; Terplan and Krauss 1969; Strich 1966; Solitare 1968; Solitare and Lopez 1967;
278 Aguilar et al. 1968a; Paula-Barbosa et al. 1983).

279 Using extracellular recording methods in the acute slice, we recorded spontaneous action potentials
280 from 3,300 PNs (**Fig. 5A**), across 188 animals, encompassing *Atm*^{R35X/R35X}; *Aptx*^{-/-} and 3 other
281 genotypes at 4 different time points (P45, 120, 210, and 400). We visually selected “healthy” cells (see
282 Methods), deeper in the slice, that consistently fired during the extent of the 60 second recording
283 period. Qualitatively, tissue and cell quality did not visually differ across genotypes under DIC
284 microscopy. Cells were sampled in a distributed fashion across the lateral, intermediate, and medial
285 (vermis) cerebellum of each mouse to assess whether changes in PN firing activity was ubiquitous or
286 anatomically restricted. Regions were segregated based on gross anatomical domains in the mouse
287 defined by natural anatomical boundaries (e.g., foliation) and their general connectivity with different
288 regions of the nervous system (e.g., forebrain, brainstem, etc.) (Voogd and Glickstein 1998).

Perez et al. Resubmission

289 We found that complete deficiency of both ATM and APTX, consistent with the behavioral results, was
290 necessary to produce a significantly reduced spontaneous PN firing frequency (**Fig. 5A, B**). Although
291 the trend of slower PN firing rates was observed across most regions of the cerebellum, some
292 subregions appeared to be less or minimally impacted, including several areas of the lateral
293 cerebellum, including the paraflocculus, paramedian, and crus I and II (**Fig. 5-fig. S1**). Significant age
294 dependent changes in firing frequency were also only observed in *Atm*^{R35X/R35X}; *Aptx*^{-/-} mice (**Fig. 5B**).
295 The most significant decline occurring between P120 and 210 [medial: 50.3 ± 2.4 Hz (n = 61) vs. 36.9 ±
296 2.2 Hz (n = 31), *t*-test, *p*=0.0006]. No significant difference in PN firing frequency was detected between
297 male and female mice within each genotype, thus the data were pooled (2-way ANOVA, *p*>0.3 across
298 all pairwise comparisons; **Fig. 5-fig. S2**). Previous studies across several mouse models of heritable
299 ataxia, including episodic ataxia and several variants of spinocerebellar ataxia find that physiological
300 disruption in PN firing not only changes its frequency, but also its regularity (Kasumu and
301 Bezprozvanny 2012; Jayabal et al. 2016; Stoyas et al. 2020; Cook, Fields, and Watt 2020). We
302 compared both the coefficient of variation (CV) and variability in adjacent intervals (CV2) between
303 *Atm*^{R35X/R35X}; *Aptx*^{-/-} and control mice (**Fig. 5-figs. S3, S4**). No difference in these parameters across
304 sex, age, or genotype was detected. Consistent with the behavioral results, cerebellar dysfunction was
305 found only in the *Atm*^{R35X/R35X}; *Aptx*^{-/-} mice that developed ataxia and not in mice with at least some
306 expression of ATM or APTX.

307 **2.5 ATM and APTX deficiency induces cerebellar atrophy**

308 Ataxia in A-T patients is usually detected between 1 to 2-years of age and is associated with mild to no
309 cerebellar atrophy (Tavani et al. 2003; Taylor et al. 2015). Significant structural changes are usually
310 apparent via neuroimaging between 5 to 10-years of age (Demaerel, Kendall, and Kingsley 1992;
311 Tavani et al. 2003). Comprehensive characterization of the progression of cerebellar atrophy is
312 however severely lacking in large part due challenges in imaging young patients (<2-years) and the
313 rarity of the disorder. We therefore assessed the gross developmental progression of cerebellar size
314 and pathohistology in mice deficient in both ATM and APTX that progressively develop a severe ataxia

Perez et al. Resubmission

315 and perturbations in cerebellar function. Structural changes in the overall size of the cerebellum were
316 examined in *Atm*^{R35X/R35X}; *Aptx*^{-/-} and several different control mice over 5 time points (P45, 120, 210,
317 400, 460; **Fig. 5C**). Cerebellar size was defined within each animal by the ratio of 2-dimensional
318 surface area of the dorsal cerebellum to the forebrain (i.e., cerebellum area divided by forebrain area).
319 The cerebellar size of control mice slightly increased during adolescence and early adulthood (P45-
320 P210), was generally stable through adulthood (P210-400), and then declined slightly in older age
321 (P400-460). In stark contrast, relative cerebellar size in *Atm*^{R35X/R35X}; *Aptx*^{-/-} mice progressively declined
322 after P120. No cerebellar atrophy was observed in mice with at least one copy of the *Atm* gene [i.e.,
323 *Atm*^{R35X/+}; *Aptx*^{-/-}; 1-way ANOVA, $F_{(3,44)} = 1.2$, $p=0.32$; **Fig. 5C**]. To rule out the possibility that reduced
324 cerebellar size was related to the smaller stature of *Atm*^{R35X/R35X}; *Aptx*^{-/-} mice, we examined, but did not
325 find a correlation between animal weight and actual cerebellar size [Pearson's correlation, $p>0.3$ for all
326 4 genotypes at P460, $n = 10$ to 20]. Furthermore, we found that cerebellar size did not differ between
327 male and the on average 22% smaller female mice across genotypes at this age [2-way ANOVA, $F_{(2,$
328 $153)} = 1.9$, $p=0.2$]. Therefore, cerebellar neurodegeneration in the *Atm*^{R35X/R35X}; *Aptx*^{-/-} mice, which begins
329 after P120, is correlated with ATM and APTX deficiency.

330 In humans, cerebellar atrophy is associated with a variety of changes in the macro-structure of the
331 cerebellar cortex and post mortem examination has identified abnormalities in the density and
332 distribution of granule cells (GC) and PNs (Verhagen et al. 2012; De Leon, Grover, and Huff 1976;
333 Amromin, Boder, and Teplitz 1979; Monaco et al. 1988; Terplan and Krauss 1969; Strich 1966; Solitare
334 1968; Solitare and Lopez 1967; Aguilar et al. 1968a; Paula-Barbosa et al. 1983; Gatti and Vinters
335 1985). In the *Atm*^{R35X/R35X}; *Aptx*^{-/-} mice we do not qualitatively observe severe pathological changes in
336 the anatomy of their cerebellum (**Fig. 5-fig. S5B**). To then understand the anatomical basis of the gross
337 atrophy, we measured the width of the cortical layer of the cerebellum that contains the massive
338 dendritic arbors of PNs called the molecular layer (ML). Consistent with the temporal changes in gross
339 cerebellar size, PN firing frequency, and behavior, ML width in *Atm*^{R35X/R35X}; *Aptx*^{-/-} mice was reduced
340 and declined in size from P120 to P400 [P400: $120.2 \pm 2.1 \mu\text{m}$ ($n = 5$) vs. $140.2 \pm 4.8 \mu\text{m}$ ($n = 5$), Sidak

Perez et al. Resubmission

341 test, $p=0.0004$; **Fig. 5D**]. In contrast, the width of the GC layer did not change with age or differ
342 significantly between *Atm*^{R35X/R35X}; *Aptx*^{-/-} and *Atm*^{+/+}; *Aptx*^{+/+} mice [P400: $135.5 \pm 2.4 \mu\text{m}$ ($n = 6$) vs.
343 $127.5 \pm 4.3 \mu\text{m}$ ($n = 5$), Sidak test, $p=0.5$; **Fig. 5D**]. These results, along with the finding that PN density
344 did not significantly differ between *Atm*^{R35X/R35X}; *Aptx*^{-/-} and *Atm*^{+/+}; *Aptx*^{+/+} mice [P400: 3.9 ± 0.3 ($n = 4$)
345 vs. 4.4 ± 0.3 ($n = 5$) PNs/4000 μm^2 , Welch's test, $p=0.3$; **Fig. 5-fig. S5B**] indicate that cerebellar atrophy
346 is largely due to a reduction in the extent of PN dendrites. At the anatomical level, we were able to
347 qualitatively observe a few other PN abnormalities. This includes abnormally large diameter primary
348 dendrites and axonal swellings in the *Atm*^{R35X/R35X}; *Aptx*^{-/-} mice (**Fig. 5-fig. S5C**). Overall, we find a good
349 correlation between the abnormal structural and electrophysiological properties and the progression of
350 motor behavioral deficits.

351 **2.6 Differential disruption of thymocyte development in ATM-deficient vs. APTX-deficient mice**

352 Chronic sinopulmonary infections associated with immunodeficiency are one of the leading causes of
353 death in A-T patients (Morrell, Cromartie, and Swift 1986; Bhatt and Bush 2014). Immunodeficiency is
354 linked to deficits in the generation of B- and T-lymphocytes that have been linked to defects in the
355 antigen receptor gene rearrangement processes during the generation of these cells in bone marrow
356 and thymus, respectively (Staples et al. 2008). The resulting defects in mature lymphocyte numbers
357 include decreases in CD4⁺ helper T-cells and killer CD8⁺ T-cells (Schubert, Reichenbach, and Zielen
358 2002). We therefore examined the percentages of T-cells in peripheral blood and of different
359 subpopulations in the thymus of *Atm*^{R35X/R35X}; *Aptx*^{-/-} mice using T-cell antigen receptor (TCR) and
360 CD4/CD8 co-receptor expression.

361 In the peripheral blood, we observed a significant reduction in the total fraction of CD3⁺ T-cells in mice
362 with reduced or absent ATM expression compared to wildtype mice (**Fig. 6**). This reduction was further
363 compounded by concomitant deficiency of APTX. ATM and APTX deficiencies reduced T-cells in
364 peripheral blood by over 65% decrease compared to wild type controls. The effect of APTX deficiency
365 was additive to that of ATM deficiency suggesting a different mechanism of action for each of these two
366 proteins on T-cell generation. The reduction in the percentage of T-cells in peripheral blood was mostly

Perez et al. Resubmission

367 associated with reduction in the CD4⁺ helper T-cell population (**Fig. 6B**). Of interest, the proportion of
368 CD8⁺ T-cells was increased only in *Atm*^{R35X/R35X}; *Aptx*^{-/-} mice (**Fig. 6B**). Again, we observed a
369 differential effect of ATM and APTX deficiencies as seen for the effects of these mutations on the total
370 T-cell fraction.

371 Given the reduction in T-cell populations in the blood, we next assessed T-cell development in the
372 thymus. In this organ, bone marrow-derived T-cell progenitors undergo TCR gene rearrangement
373 followed by positive selection for MHC restriction and negative selection of autoreactive clones. The
374 phases of thymocyte development can be followed by monitoring expression of CD4 and CD8
375 expression in thymocytes. The progression of this developmental program goes from double negative
376 (CD4⁻CD8⁻) thymocytes, to double positive (CD4⁺CD8⁺) thymocytes and then to single positive (CD4⁺ or
377 CD8⁺) thymocytes. In addition, within the double negative stage, four different subpopulations can be
378 identified, based on expression of CD25 and CD44, known as DN1 (CD44⁺CD25⁻), DN2
379 (CD44⁺CD25⁺), DN3 (CD25⁺CD44⁻) and DN4 (CD44⁻CD25⁻) (Germain 2002).

380 Gene rearrangement during thymocyte development occurs twice, once at the double negative
381 thymocyte stage in the CD25⁺CD44⁻ stage (Krangel 2009) and then again in double positive thymocyte
382 stage before progressing into separate CD4⁺ and CD8⁺ single positive populations (Livák et al. 1999).
383 ATM deficiency has been linked to defects in both bouts of rearrangement in mice (Vachio 2007,
384 Hathcock 2013). Therefore, we compared the proportion of cells in the thymus expressing these
385 different developmental cell surface markers in our ATM deficient and control mice (**Fig. 7**).
386 *Atm*^{R35X/R35X}; *Aptx*^{-/-} and *Atm*^{R35X/+}; *Aptx*^{-/-}, but not *Atm*^{R35X/R35X}; *Aptx*^{+/+} mice had significantly elevated
387 proportions of CD44⁺CD25⁻, CD44⁺CD25⁺, and CD44⁻CD25⁺ cells compared to wildtype (**Fig. 7A**).
388 These increased proportions appear to be due in part to an impediment of CD44⁻CD25⁺ cells maturing
389 into CD44⁻CD25⁻ double negative cells, as the fraction of cells from *Atm*^{R35X/R35X}; *Aptx*^{-/-} and *Atm*^{R35X/+};
390 *Aptx*^{-/-} mice is significantly lower than wildtype (**Fig. 7A**). Of interest, APTX deficiency by itself had the
391 greatest effect on the loss of DN4 cells suggesting that APTX deficiency, rather than ATM deficiency, is

Perez et al. Resubmission

392 responsible for this effect. To our knowledge, this finding implicates for the first time APTX in gene
393 rearrangement during the process of TCR β recombination.

394 Next, we looked at the proportions of CD4⁺CD8⁺ thymocytes compared to CD4⁺CD8⁻ and CD4⁻CD8⁺
395 single positive thymocytes in these four different strains. In agreement with our results in the blood and
396 prior studies, we found that ATM-deficient mice but not control mice displayed decreased expression of
397 CD4⁺CD8⁻ and CD4⁻CD8⁺ single positive thymocytes (**Fig. 7B**). These results support the role of ATM
398 in TCR α/δ gene rearrangement during thymocyte development (Bredemeyer et al. 2006), a role that is
399 independent of the role played by APTX in early thymocyte maturation.

400 **2.7 Readthrough molecules overcome PTC to restore ATM expression**

401 Our primary rationale for inserting a clinically relevant nonsense mutation in the *Atm* gene was to
402 generate a mouse amenable to critical pre-clinical testing of a novel set of small molecule readthrough
403 (SMRT) compounds. We previously demonstrated SMRT compounds recover production of ATM
404 protein in A-T patient derived lymphoblastoid cell lines by overcoming premature termination codons
405 (PTC) caused by nonsense mutations (Du et al. 2013). To demonstrate suitability of this new A-T
406 animal model for SMRT compound testing we chose to directly examine their ability to restore ATM
407 expression using an explant approach that circumvents challenges related to *in vivo* delivery (e.g.,
408 bioavailability, route of delivery, etc.). ATM expression was measured in samples from the spleen,
409 where ATM is normally expressed at high levels, and the cerebellum, a key target tissue for the
410 disorder. We exposed these explant tissues, harvested from homozygous *Atm*^{R35X} and *Atm*^{Q35X} mice
411 with either a candidate SMRT compound (GJ103), or an aminoglycoside previously known to have
412 readthrough properties (G418) for 72 hrs. and then measured ATM expression by immunoblot to
413 assess restoration. In both types of ATM deficient mice, ATM expression was consistently restored in
414 the spleen and cerebellum by both G418, GJ103 (**Fig. 8**). These results demonstrate that our SMRT
415 compounds can enable readthrough of at least 2 of the 3 possible nonsense mutation causing PTCs
416 and provide the rationale for *in vivo* efficacy testing in follow-on studies.

Perez et al. Resubmission

417 3.0 Discussion

418 By increasing genotoxic stress through the addition of a secondary hit to the DDR pathway, we
419 generated a novel mouse model that displays the most comprehensive set of A-T symptoms of any
420 model to date. This includes a severe and progressive ataxia associated with cerebellar atrophy and
421 perturbations of PN properties along with a high incidence of cancer and defects in immune cell
422 development. Together, these comorbidities encompass the three leading causes of premature death in
423 A-T — each contributing to roughly a third. Of these, the incapacitating effect of ataxia is the most
424 penetrant and is reported by patients and caregivers as having the greatest impact on their quality of
425 life. For this reason, the presence of ataxia and cerebellar atrophy in this new mouse model is of great
426 significance as it provides for the very first time a resource to not only elucidate the mechanisms of
427 neurological dysfunction, but also a critically needed *in vivo* model to test severely needed A-T
428 therapeutics like the readthrough compounds we describe here.

429 We found several similarities between the overall progression of ataxia in the *Atm*^{R35X/R35X}; *Aptx*^{-/-} mice
430 and A-T patients. In clinical A-T, motor deficits are observable by roughly 2-years of age, when parents
431 and doctors detect a lowered ability to transition from toddling to a smooth, reflexively coordinated
432 gate—unfortunately, little is known about motor defects at earlier stages due to the diseases low
433 prevalence and current lack of early diagnostic testing (Rothblum-Oviatt et al. 2016). Patients usually
434 learn to walk without assistance and neurological symptoms tend to remain stable through the first 4 to
435 5 years of life (Rothblum-Oviatt et al. 2016). We found a similar early progression of motor deficits in
436 *Atm*^{R35X/R35X}; *Aptx*^{-/-} mice, detecting mild motor deficits early at P8 (righting reflex deficit), followed by a
437 period of relative stability, prior to onset of a progressive and severe ataxia developing after p210 that
438 included changes in gait, startle reflex, tremor, and locomotor activity. Several important questions arise
439 out of these findings, including whether ATM and/or APTX have a neurodevelopmental role in the
440 cerebellum. Future studies focused on the early phase of the disorder will be critical in understanding if
441 the cerebellum develops normally prior to dysfunction or whether developmental defects are an initial
442 cause. We also found, similar to A-T patients, that the severity of the late developing ataxia was

Perez et al. Resubmission

443 variable with some mice ambulating with a clumsy, high stepping rear gate (**Video 3**) and others
444 moving almost entirely via contortion of the rear trunk (**Fig. 1E** and **Video 4**) (Rothblum-Oviatt et al.
445 2016; Levy and Lang 2018; Boder and Sedgwick 1958). Overall, we found that *Atm*^{R35X/R35X}; *Aptx*^{-/-} mice
446 developed a visually profound and measurable progressive loss in motor coordination that was similar
447 to that observed in A-T patients and that was rescued by expression of at least one copy of the *Atm* or
448 *Aptx* gene.

449 The loss of motor coordination in A-T has been attributed to cerebellar degeneration due to its relatively
450 selective neuropathology across the brain and its causal role in several different forms of ataxia (Hoche
451 et al. 2012). Consistent with A-T patient neuroimaging studies (Wallis et al. 2007; Sahama et al. 2015;
452 Sahama et al. 2014; Dineen et al. 2020; Tavani et al. 2003; Quarantelli et al. 2013), we find that
453 cerebellar size in *Atm*^{R35X/R35X}; *Aptx*^{-/-} mice is initially normal, but progressively atrophies in line with
454 changes in neurological function. While loss of cerebellar tissue has been considered a main cause of
455 ataxia in humans, it is unclear from clinical data if ataxia severity is a good predictor of the extent of
456 cerebellar degeneration found postmortem (Aguilar et al. 1968b; Crawford et al. 2006; Dineen et al.
457 2020). In the *Atm*^{R35X/R35X}; *Aptx*^{-/-} mice, we find clear atrophy associated with thinning of the Purkinje
458 neuron dendrite layer that precedes the late, severe behavioral deficits. However, since the
459 neuropathology observed in the *Atm*^{R35X/R35X}; *Aptx*^{-/-} mice is not severe, our findings suggest that like
460 several SCAs (e.g., 1 and 3), changes in cerebellar function itself, rather than profound loss of
461 cerebellar cells, is likely sufficient to cause the ataxic phenotype (Shakkottai et al. 2011b; Lorenzetti et
462 al. 2000; Clark et al. 1997).

463 Why ATM and APTX deficiency is required to generate ataxia in mice, when loss of either is sufficient
464 to cause ataxia in humans, remains unclear. One possibility is that the rodent brain may more flexibly
465 utilize compensatory pathways or redundant proteins while responding to the 10-20k DNA lesions that
466 impact cells each day (Lindahl and Barnes 2000). Several forms of DNA repair exist to potentially meet
467 this challenge, including base excision repair (BER), nucleotide excision repair (NER), as well as
468 homologous and non-homologous end joining (HEJ and NHEJ, respectively), all of which ATM and

Perez et al. Resubmission

469 APTX have been implicated in (Chou et al. 2015; Çaglayan et al. 2017; Wakasugi et al. 2014; Tumbale
470 et al. 2018; Chatterjee and Walker 2017). Alternatively, it may be the case that deficiency in ATM or
471 APTX alone does not adequately impact cell health during the mouse's comparatively short lifespan,
472 and thus eliminating both proteins is necessary to achieve sufficient accumulation of DNA damage to
473 manifest over this time period. This possibility is strengthened by the fact that ATM and APTX have
474 distinct biochemical properties and functional roles in the DNA damage response, and therefore
475 deficiency in both would be predicted to cause a broader hit to genome stability (i.e., increased
476 genotoxic stress).

477 Our finding, that two genome stability pathway proteins are required to induce neurological defects in
478 mice strongly suggests that it is the loss of ATM's role in DNA repair, rather than potential functions in
479 oxidative stress signaling, mitophagy, or mitochondrial function that cause the cerebellar defects
480 (Shiloh 2020). Alternatives however, cannot be completely ruled out, as APTX, like ATM has been
481 observed within the mitochondria of brain cells, where it is thought to support the processing of
482 mitochondrial DNA (Meagher and Lightowlers 2014; Sykora et al. 2011). This new mouse model
483 provides a new tool to explore these possibilities and mechanistically define how loss of ATM and
484 APTX ultimately causes cerebellar dysfunction.

485 The biophysical perturbations observed in PNs recorded from the *Atm*^{R35X/R35X}; *Aptx*^{-/-} mice are similarly
486 found in several other mouse models of ataxia. This includes changes we observed in PN input
487 resistance, membrane capacitance, and AP threshold and width, which have also been described in
488 mouse models of SCA like 1, 3, and 7 (Stoyas et al. 2020; Shakkottai et al. 2011b; Dell'Orco et al.
489 2015). Moreover, the progressive reduction in PN action potential firing frequency we report, which
490 correlates well with the development of ataxia in the *Atm*^{R35X/R35X}; *Aptx*^{-/-} mice, is reported in a large
491 number of ataxic mouse models, including SCAs 1, 2, 3, 5, 6, and 13 as well as a few episodic forms
492 (see review (Cook, Fields, and Watt 2020)).

493 Given the significant overlap in PN perturbations observed across many different ataxias caused by
494 distinct cellular defects, restoring PN AP firing frequencies has been considered as a broad-based

Perez et al. Resubmission

495 therapeutic approach. However, it remains unclear whether reduced PN firing is an actual causal factor
496 of ataxia. Moreover, experimental evidence suggests changes in PN activity may in fact be a
497 generalized response to maintain homeostasis during ongoing disease-related impairment of PN
498 physiology (Dell'Orco et al. 2015). Thus, continued efforts across all cerebellar ataxias are needed to
499 link the genetic, molecular, and cellular disruptions caused by disease to the specific changes in
500 cerebellar neural signaling that ultimately generates the ataxia. Of significant importance in this effort
501 will be defining whether disease-causing cerebellar defects commonly or differentially cause ataxia
502 through a loss of cerebellar function (e.g., loss of coordinating signals during movement), or from a
503 dominant negative effect (e.g., disrupting downstream neural circuits with abnormal neural output
504 patterns). Ultimately, while a common therapeutic strategy to address cerebellar ataxias would have the
505 greatest impact, a directed approach that addresses the distinct genetic and molecular causes of
506 cellular dysfunction may ultimately be necessary to successfully develop an efficacious therapeutic.

507 The mechanistic link between deficiency in DNA stability proteins like ATM and APTX and PN
508 dysfunction is far less obvious than it is for other types of ataxia, like the loss of voltage gated ion
509 channels that directly shape membrane excitability in SCA6 (i.e., $Ca_{v2.1}$) (Jayabal et al. 2016). Our
510 results suggest the effects of ATM and APTX loss on PNs is intrinsic, as we don't find changes in the
511 presynaptic properties of granule cells, nor evidence of their cellular loss (no change in GCL thickness).
512 Moreover, while we observed differences in short term plasticity of inferior olivary inputs in ATM and
513 APTX deficient PNs and wildtype, these results likely point to a disruption in Ca^{2+} homeostasis
514 potentially via reductions in Inositol 1,4,5-triphosphate receptor 1 (*Itpr1*) expression, similar to those
515 observed in SCAs 1, 2, and 3 mouse models as well as ATM-deficient mice (Kim et al. 2020; Chen et
516 al. 2008; Liu et al. 2009; Shakkottai et al. 2011b). While this provides a promising avenue for future
517 examination and comparison, it is as of yet unclear, even for the SCAs, whether changes in Ca^{2+}
518 homeostasis is the causal factor or just another symptom or even compensatory response of diseased
519 or disturbed PNs (Dell'Orco et al. 2015).

Perez et al. Resubmission

520 In the immune system, ATM is implicated in the repair of DNA breaks that naturally occur during gene
521 rearrangement of antigen receptor genes in B- and T-cell precursors, a phenomenon critical for antigen
522 receptor (Ig and TCR) diversity of these cells. Our finding that T-cell proportions in the blood are
523 significantly reduced is consistent with prior studies in humans and A-T knockout mice (Schubert,
524 Reichenbach, and Zielen 2002; Hathcock et al. 2013; Chao, Yang, and Xu 2000; Barlow et al. 1996).
525 This reduction of T-cells in the periphery likely correlates with a defect in both cellular and humoral
526 immunity. Importantly, we found that expression of at least one copy of the ATM gene is enough to
527 restore CD4⁺ deficits in the blood indicating that therapies able to restore at least some ATM
528 expression would have therapeutic efficacy. Although we have not assessed B-cell development in this
529 paper, it is likely that similar conclusions would apply to that process given their mechanistic similarities
530 (Marshall et al. 2018).

531 As expected, the reduction of T-cells in peripheral blood correlated with defective thymocyte
532 development. In the thymus, we found two main defects. One, induced primarily by APTX deficiency,
533 manifests as a defect in the DN3 to DN4 transition coinciding with early rearrangement of TCR β locus.
534 The other defect, primarily caused by ATM deficiency, correlates with decreased progression of double
535 positive CD4⁺CD8⁺ to single positive cells, primarily CD4⁺ thymocytes. While the APTX finding was
536 surprising, as its deficiency (AOA 1) is not associated with immune deficits, APTX is known to interact
537 with TCR β gene rearrangement proteins, including XRCC4 (Clements et al. 2004). Future studies
538 aimed at defining APTX's role in end-joining mechanisms during TCR gene rearrangement will be
539 important, and the possibility that alternative end-joining mechanisms, like the use of microhomologies
540 account for the lack of an immune deficit in its absence need further investigation (Bogue et al. 1997).

541 The survivability of *Atm*^{R35X/R35X}; *Aptx*^{-/-} mice is considerably longer than prior A-T mouse models. In
542 comparison, the first A-T KO mouse model reported by Barlow et al. died from thymomas usually within
543 2-4 months after birth (Barlow et al. 1996). The increased severity of cancer survivability in this, and
544 many other knockout A-T mouse models is likely genetic, as the background strain harboring the
545 mutation has been shown to have significant effects on cancer prevalence and survivability, with A/J

Perez et al. Resubmission

546 and C57BL/6 backgrounds having significantly increased survivability over the BALBC and 129S strains
547 (Genik et al. 2014). The fact that our ATM deficient mice were created on a C57BL/6 background likely
548 underlies their comparatively long lifespan. Given that the *Atm*^{R35X/R35X}; *Aptx*^{+/+} mice do not develop
549 ataxia, it is unlikely that the early death in A-T KO mice prevents observation of an ataxic phenotype
550 that would otherwise develop in these mice. On the other hand, it is unknown whether the C57BL/6
551 background confers a resilience to developing ataxia, as it does for cancer. Defining the genetic or
552 possibly epigenetic factors that influence the severity of the disease could provide avenues for future
553 therapeutic development.

554 Given the global nature of the ATM and APTX null mutation in our mouse model, we cannot entirely
555 rule out that extra-cerebellar defects may also contribute to the severe ataxic phenotype, and thus
556 future examination outside the cerebellum, in both the forebrain, brainstem, spinal cord, and even
557 muscle will need to be conducted. Within the cerebellum, while we found some anatomical differences
558 in the PN firing properties within different regions of the cerebellum, we didn't detect regional
559 differences in ML width or PN density. However, there are challenges in using regional anatomy as a
560 grouping factor in the cerebellum, as the physical folds of the tissue do not necessarily correlate with
561 the boundaries of functional, molecular expression, or biophysical property domains that have been
562 described (Apps and Hawkes 2009; Tsutsumi et al. 2015; Gao, van Beugen, and De Zeeuw 2012; Zhou
563 et al. 2014). Experiments focused on examining the extent of cerebellar defects within these domains
564 will be important in future studies and compared to the anecdotal reports of anatomical differences in A-
565 T patients (Verhagen et al. 2012; De Leon, Grover, and Huff 1976; Amromin, Boder, and Teplitz 1979;
566 Monaco et al. 1988; Terplan and Krauss 1969; Strich 1966; Solitare 1968; Solitare and Lopez 1967;
567 Aguilar et al. 1968a; Paula-Barbosa et al. 1983).

568 While we detect two potential stages in the progression of ataxia in the *Atm*^{R35X/R35X}; *Aptx*^{+/+} mice, the
569 later stage of severe ataxia develops in adulthood in mice, as compared to the childhood onset in
570 humans. This may limit its use in some neurodevelopmental based studies. Also, the interpretation of
571 future experiments must carefully factor in the fact that this new model expresses null mutations in two

Perez et al. Resubmission

572 genome stability genes at the same time, a situation that has not been detected in human patients with
573 either A-T or AOA1.

574 Finally, pinpointing where, when, and how ATM deficiency causes cerebellar pathology and ataxia has
575 been a challenge as prior ATM deficient mice generally lack the characteristic features needed to
576 causally link cellular and molecular deficits to the ataxic phenotype. Multiple promising avenues of
577 investigation have been defined, including those focused at the neuronal level where ATM is implicated
578 in oxidative stress signaling (Chen et al. 2003) and synaptic function (Li et al. 2009; Vail et al. 2016), as
579 well as glial function, where recent evidence suggests glial pathology may be a leading factor in
580 cerebellar pathology (Kaminsky et al. 2016; Campbell et al. 2016; Petersen, Rimkus, and Wassarman
581 2012; Weyemi et al. 2015). This novel animal model provides a new tool to test mechanistic
582 hypotheses regarding how ATM deficiency causes cerebellar pathology and ataxia. Additionally, this
583 model may serve most importantly as a critical preclinical tool for testing both previously proposed
584 therapeutic candidates (Browne et al. 2004; Chen et al. 2003) and our own SMRT compounds (Du et
585 al. 2013). The severe limitations of not having a suitable preclinical model for therapeutic testing,
586 especially for a rare disorder like A-T and AOA1, cannot be overstated.

587 4.0 Materials and Methods

Key Resources Table				
Reagent type (species) or resource	Designation	Source or reference	Identifiers	Additional information
Strain, strain background (<i>Mus musculus</i>)	<i>Atm</i> ^{R35X} , <i>Atm</i> ^{Tm1.1(103 CAG)TGA} <i>Mfgc</i>	This paper	103C>T mutation, human exon replacement	Generated by Hicks laboratory. Has been backcrossed into C57b/6 9 times. Contact pmathews@lundquist.org

Perez et al. Resubmission

Strain, strain background (<i>Mus musculus</i>)	<i>Atm</i> ^{Q35X} <i>Atm</i> ^{Tm1.1(103C)} <i>TJ</i> ^{Mfgc}	This paper	103C>T mutation, targeted premature termination signal in the mouse codon	Generated by Hicks laboratory. Has been backcrossed into C57b/6 9 times. Contact pmathews@lundquist.org
Strain, strain background (<i>Mus musculus</i>)	<i>Aptx</i> ^{-/-}	Ahel et al. 2006	MGI Cat# 3687171, RRID:MGI:3687171	Contact peter.mckinnon@stjude.org
Gene (<i>Mus musculus</i>)	<i>Atm</i>	MGI	MGI:107202; C030026E19 Rik; ENSMUSG0000034218	
Gene (<i>Homo Sapien</i>)	<i>ATM</i>	OMIM	OMIM: 607585 MGI: 107202 HomoloGene: 30952; ENSG00000149311	
Sequence-based reagent	<i>Atm</i> gene	Transnetyx	PCR primers	F-5'- CCTTTGAG GCATAAGT TGCAACTT G-3'
Sequence-based reagent	<i>Atm</i> gene	Transnetyx	PCR primers	R- 5'- GTACAGTGT ATCAGGTTA GGCATGC-3'
Chemical compound/ drugs	GJ103 salt Formula: <chem>C16H14N4O3S</chem>	TargetMol	T3448; CAS No. : 1459687-96-7	100 μM in media
Antibody	ATM (D2E2) (Rabbit-monoclonal)	Cell Signaling Technology	Cell Signaling Technology Cat# 2873, RRID:AB_206	WB(1:500) WB(1:1000)

Perez et al. Resubmission

			2659	
Antibody	GAPDH (14C10) (Rabbit- monoclonal)	Cell Signaling Technology	Cell Signaling Technology Cat# 2118, RRID:AB_561 053	WB(1:4000)
Antibody	β -Actin (D6A8) (Rabbit- monoclonal)	Cell Signaling Technology	Cell Signaling Technology Cat# 8457, RRID:AB_109 50489	WB(1:5000)
Antibody	Anti-Rabbit IgG,HRP- linked (Goat- monoclonal- polyclonal)	Cell Signaling Technology	Cell Signaling Technology Cat# 7074, RRID:AB_209 9233	WB(1:5000)
Antibody	Calbindin (D-28k) (Rabbit, polyclonal)	Swant Inc.	Swant Cat# CB 38, RRID:AB_100 00340	IF (1:1000)
Antibody	Anti-Rabbit Alexa Fluor 488 (Goat- polyclonal)	ThermoFisher Invitrogen	Thermo Fisher Scientific Cat# A- 11034, RRID:AB_257 6217	IF(1:1000)
Antibody	CD4 (GK1.5) (Rat- monoclonal)	ThermoFisher Invitrogen	Thermo Fisher Scientific Cat# 50- 0041-82, RRID:AB_106 09337	FACS (5 ul per test)
Antibody	CD8 (53-6.7) (Rat- monoclonal)	ThermoFisher Invitrogen	Thermo Fisher Scientific Cat# 53- 0081-82, RRID:AB_469 897	FACS (5 ul per test)

Perez et al. Resubmission

Antibody	CD3 (145-2C11) (Hamster- monoclonal)	ThermoFisher Invitrogen	Thermo Fisher Scientific Cat# 12- 0031-83, RRID:AB_465 497	FACS (5 ul per test)
Antibody	CD44 (IM7) (Rat- monoclonal)	ThermoFisher Invitrogen	Thermo Fisher Scientific Cat# 25- 0441-82, RRID:AB_469 623	FACS (5 ul per test)
Antibody	CD25 (PC61.5) (Rat- monoclonal)	ThermoFisher Invitrogen	Thermo Fisher Scientific Cat# 47- 0251-82, RRID:AB_127 2179	FACS (5 ul per test)
Other	Fluoromount -G with DAPI	Southern Biotech	Cat# 0100-20, RRID: SCR_021261	
Commercial assay or kit	BCA Protein Assay Kit	ThermoFisher Pierce	Cat# 23225	Protein Assay
Commercial assay or kit	SuperSignal West Pico Chemilumine scent Substrate	ThermoFisher Pierce	Cat# 34580	Chemilumine scent Substrate
Commercial assay or kit	Radiance plus	Azure Biosystems	Cat# AC2103	Chemilumine scent Substrate
Software, algorithm	FlowJo	https://www.fl owjo.com/solu tions/flowjo	RRID:SCR_0 08520	
Software, algorithm	ImageJ software	ImageJ (http://imagej. nih.gov/ij/)	RRID:SCR_0 03070	

Perez et al. Resubmission

Software, algorithm	IgorPro	http://www.wavemetrics.com/products/igorpro/igorpro.htm	RRID: SCR_000325	Version 7; Tarotools procedures
Software, algorithm	Neuroexpress	https://www.researchgate.net/project/NeuroExpress-Analysis-software-for-whole-cell-electrophysiological-data	https://www.researchgate.net/project/NeuroExpress-Analysis-software-for-whole-cell-electrophysiological-data	Version 21.1.13; Used for mEPSC analyses
Software, algorithm	GraphPad, Prism	GraphPad Prism (https://graphpad.com)	RRID: SCR_015807	Versions 8 and 9
Software, algorithm	MBF, Stereo investigator	https://www.mbfbioscience.com/stereology	RRID: SCR_017667	Version 2021
Software, algorithm	Microsoft Excel	https://www.microsoft.com/en-us/microsoft-365/excel	RRID: SCR_016137	Version 365
Software, algorithm	Catwalk XT	https://www.noldus.com/catwalk-xt	RRID: SCR_021262	

588

589 **4.1 Ethics Statement**

590 This study was performed in strict accordance with the recommendations in the Guide for the Care and
 591 Use of Laboratory Animals of the National Institutes of Health. All the animals were handled according
 592 to approved institutional animal care and use committee (IACUC) protocols at The Lundquist Institute
 593 (31374-03, 31773-02) and UCLA (ARC-2007-082, ARC-2013-068). The protocol was approved by the
 594 Committee on the Ethics of Animal Experiments of the Lundquist Institute (Assurance Number: D16-
 595 00213). Every effort was made to minimize pain and suffering by providing support when necessary
 596 and choosing ethical endpoints.

Perez et al. Resubmission

597 **4.2 Mice**

598 All mice were group housed and kept under a 12-h day/night cycle with food and water available *ad*
599 *libitum*. Animals were housed within the general mouse house population, and not in specialized
600 pathogen free rooms. Older animals were made available wetted food or food gel packs on the ground
601 of the cages as ataxia developed. *Atm*^{R35X} and *Atm*^{Q35X} mice were created and provided by Dr. Hicks
602 and colleagues at the University of Manitoba.

603 These mice were created to contain the c.103C>T mutation found in a large population of North African
604 AT patients, using recombineering Gateway technology and site-directed mutagenesis. A C>T mutation
605 at this position in the mouse *Atm* gene creates a TAG G stop codon. The same mutation in the human
606 ATM gene produces a TGA G stop codon. In consideration of the use of these models for therapeutic
607 interventions, we chose to create a mouse model for each of the two PTC codons (**Fig. 1A**).

608 A modified Gateway R3-R4-destination vector was used to pull out the desired region of the mouse *Atm*
609 gene from a Bacterial Artificial Chromosome (BAC) and subsequently mutated to create either a TAG G
610 stop codon at codon 35 (M00001, position 103 (C>T)) or a TGA G stop codon (M00002, position 103
611 (CAG>TGA), replicating the human AT PTC). The genomic alleles were then cloned into a modified
612 version of the NorCOMM mammalian targeting vector using a 3-way Gateway Reaction (Bradley et al.
613 2012). The resulting targeting vectors were electroporated into C2 ES cells (C57Bl/6N, derived in A.
614 Nagy lab, Toronto, Canada) and successfully targeted clones were identified by selection with G418
615 (Gertsenstein et al. 2010). Integration of the mutated targeting cassette into the *Atm* gene locus was
616 confirmed by Southern blot, and by sequencing of PCR products to confirm the presence of the *Atm*
617 PTC mutation, error free targeting into the *Atm* locus and error free functional components of the vector
618 (data not shown). Positive ES clones were used for blastocyst injection to obtain the transgenic lines.
619 The transgenic allele contained a floxed human beta actin promoter - delta TK1- Neo cassette in the
620 intron upstream of the region containing the mutated exon. This floxed cassette was subsequently
621 excised by crossing with a Cre driver mouse (B6.C-Tg(CMV-cre)1Cgn/J) to generate *Atm*^{R35X/+} and
622 *Atm*^{Q35X/+} (MGI nomenclature: *Atm*^{TM1(103CAG>TGA)MFGC} and *Atm*^{TM1(103C>T)MFGC}, respectively) mouse lines

Perez et al. Resubmission

623 **(Fig. 1A)**. Genotyping of the two *Atm* lines was performed by using the following primers at Tm 62°C:
624 *Atm* gene forward (F) primer: 5'-CCTTTGAGGCATAAGTTGCAACTTG-3'; and *Atm* gene reverse (R)
625 primer: 5'-GTACAGTGTATCAGGTTAGGCATGC-3', creating a Wild-type allele product of 151bp or
626 targeted allele product of 241bp (**Figs. 1A, 1B**).

627 *Atm*^{R35X} and *Atm*^{Q35X} were backcrossed with C57Bl/6J mice for 9 generations (99.2% isogenic) prior to
628 cryopreservation and subsequent rederivation using C57Bl/6J surrogate mothers. *Atm*^{R35X} and *Atm*^{Q35X}
629 breeders were obtained from F1 sibling *Atm*^{R35X/+} and *Atm*^{Q35X/+} mice. *Atm*^{R35X/R35X} and *Atm*^{Q35X/Q35X} were
630 both found to be fertile. *Aptx* knockout (*Aptx*^{-/-}) mice were created and provided to Dr. Mathews as
631 embryos from Dr. McKinnon (Ahel et al. 2006), and subsequently rederived via C57Bl/6J surrogate
632 mothers. *Aptx*^{-/-} mice are on a C57Bl/6 and 129 mixed background. *Atm*^{R35/R35XX}; *Aptx*^{-/-} mice of various
633 wildtype, heterozygous, and homozygous combinations were created from *Atm*^{R35X/+}; *Aptx*^{+/-} breeders
634 generated by crossing *Atm*^{R35X/R35X} and *Aptx*^{-/-} mice. One cohort of double mutant and corresponding
635 control mice were used in the longitudinal behavioral study for gait analyses and SHIRPA testing (**Figs.**
636 **2, 3**). Multiple additional cohorts of age matched double mutant and control mice were used for
637 electrophysiological, immunohistological, and Vertical Pole test experiments (**Figs. 4, 7**). Immunological
638 and protein expression experiments were carried out using mice bred from the original *Atm*^{R35X} and
639 *Atm*^{Q35X} rederived mice (**Figs. 5, 6, and 8**).

640 Genotyping was performed from ear tissue samples of P8-11 mice. Real-time PCR methods conducted
641 by Transnetyx Inc. were used to determine each animals' genotype. Animals were made identifiable via
642 toe tattoos given at the same time as ear biopsy. Unique primers for *Atm*^{R35X} and *Atm*^{Q35X} were
643 quantified and used to identify wildtype, hetero- and homo-zygous mice (listed above). *Aptx*^{-/-} and
644 *Aptx*^{+/+} primers were used to assess their genotypes.

645 **4.3 Animal Health**

646 Animals were weighed via a digital scale at P8, 45, 120, 210, 400. Animal death was recorded as the
647 day found dead, or on the day of euthanization when the animals reached a humane endpoint (animal
648 unable to right itself within 60s, significant hair matting indicating lack of self-grooming, or excessive

Perez et al. Resubmission

649 distress as noted by the veterinary staff). Animal carcasses were immediately frozen upon death, and
650 postmortem necropsies were carried out in batch. Probable cause of death was determined to the best
651 of our ability in collaboration with the staff veterinarian (Dr. Catalina Guerra) by visual inspection of the
652 internal organs. Some mice were cannibalized or accidentally disposed of by vivarium staff and were
653 therefore labelled as “missing.” Mice with no discernable visual cause of death were labelled
654 “indeterminable.” Mice that were found with thoracic masses near where the thymus would normally be
655 in young mice were listed as “thymic cancer.” All other identified probable causes of death (e.g.,
656 enlarged livers, urinary blockage) were labelled “other.”

657 **4.4 Behavior**

658 Before performing any behavioral test, mice were acclimated to the behavioral suite for ~20-minutes.
659 Mice were tested at varying times of the day, in line with their day cycle. A battery of behavioral tests
660 was performed on naïve double mutant mice of the indicated genotypes at various time points
661 depending on the behavior but in the same cohort of mice. The battery of tests included Catwalk Gait
662 assessment (P45, 120, 210, 400) and a subset of the SmithKline-Beecham Harwell Imperial-College
663 and Royal-London-Hospital Phenotype Assessment (SHIRPA) tests (P30 and 400). These tests were
664 conducted by the UCLA Behavioral Core. Double mutant and control mice were additionally examined
665 on the Vertical Pole test. All behavioral apparatus was wiped down with ethanol (70%) between each
666 testing each subject.

667 Gait Analysis

668 We used a Noldus Catwalk Gait analysis system designed to semi-automatically measure and analyze
669 the gait of mice during normal ambulation. Briefly, the movement of mice across a glass bottom corridor
670 is video recorded from a ventral position. Paw prints are highlighted in the video due to light illumination
671 across the glass walking platform. Each mouse step within a video is subsequently detected using
672 Catwalk XT (Noldus) in a semi-automated fashion. A run for each mouse consists of 3 trials of
673 consistent ambulation across the monitored platform. Only consistent trials are accepted, and mice may
674 take up to 10 attempts to complete 3 compliant trials in either direction across the corridor. Compliant

Perez et al. Resubmission

675 trials were defined as those with movement across the platform under 5 s-long and with no more than
676 60% speed variation. Once placed onto the platform, mice generally ran back and forth without any
677 need for experimenter prompting.

678 Vertical Pole

679 Mice are placed at the top of an 80 cm tall bolt with their nose faced down and hind paws as close to the
680 top as possible. Mice are immediately released, and time started immediately upon placement. Time is
681 stopped when the first forepaw touches the surface below the pole. A mouse's natural predilection is to
682 immediately climb down the pole, and they are given up to 60 s to traverse the pole, otherwise they are
683 helped off the pole. A non-completed trial is automatically given a time of 30 s, as 95% of mice that did
684 not descend within 30 s were still on the pole at the 60 s mark.

685 SHIRPA

686 Behavioral tests were conducted by the University of California, Los Angeles Behavioral Core at P30
687 and P400. All parameters are scored to provide a quantitative assessment, which enables comparison
688 of results both over time and between different laboratories. Each mouse was sequentially tested
689 across all behaviors within ~20-min time span before moving onto the next mouse. The experimenter
690 was blinded to animal genotype. The screen was performed as described previously (Rogers et al.
691 1997).

692 *Behavioral Observation*

693 The primary screen provides a behavioral observation profile and assessment of each animal begins by
694 observing undisturbed behavior in a viewing jar (10 cm diameter) for 5-min. In addition to the scored
695 behaviors of **body position**, **spontaneous activity**, **respiration rate**, and **tremor**, the observer logs
696 any instances of bizarre or stereotyped behavior and convulsions, compulsive licking, self-destructive
697 biting, retropulsion (walking backwards) and indications of spatial disorientation.

698 *Arena Behavior*

Perez et al. Resubmission

699 Thereafter, the mouse is transferred to the arena (30 cm x 50 cm) for testing of transfer arousal and
700 observation of normal behavior. The arena is marked into a grid of 10 cm² squares to measure
701 locomotor activity within a 30 s-period. While the mouse is active in the arena, measures of **startle**
702 **response, gait, pelvic elevation, and tail elevation** are recorded.

703 *Supine Restraint*

704 The animal is restrained in a supine position to record autonomic behaviors. During this assessment,
705 **grip strength, body tone, pinna reflex, corneal reflex, toe pinch, wire maneuver, and heart rate,**
706 were evaluated.

707 *Balance and Orientation*

708 Finally, several measures of vestibular system function were performed. The **righting reflex, contact**
709 **righting reflex, and negative geotaxis** tests were performed. Throughout this procedure vocalization,
710 urination and general fear, irritability, or aggression were recorded.

711 *Equipment Used*

- 712 1. Clear Plexiglas arena (approximate internal dimensions 55 x 33 x 18 cm). On the floor of the arena
713 is a Plexiglas sheet marked with 15 squares (11 cm). A rigid horizontal wire (3 mm diameter) is
714 secured across the rear right corner such that the animals cannot touch the sides during the wire
715 maneuver. A grid (40 x 20 cm) with 12 mm mesh (approximate) is secured across the width of the
716 box for measuring tail suspension and grip strength behavior.
- 717 2. A clear Plexiglas cylinder (15 x 11 cm) was used as a viewing jar.
- 718 3. One grid floor (40 x 20 cm) with 12 mm meshes on which viewing jars stand.
- 719 4. Four cylindrical stainless-steel supports (3 cm high x 2.5 cm diameter) to raise grids off the bench.
- 720 5. One square (13 cm) stainless steel plate for transfer of animals to the arena.
- 721 6. Cut lengths of 3 / 0 Mersilk held in the forceps for corneal and pinna reflex tests
- 722 7. A plastic dowel rod sharpened to a pencil point to test salivation and biting.
- 723 8. A pair of dissecting equipment forceps, curved with fine points (125 mm forceps, Philip Harris
724 Scientific, Cat. No. D46-174), for the toe pinch.

Perez et al. Resubmission

- 725 9. A stopwatch.
- 726 10. An IHR Click box is used for testing the startle responses. The Click Box generates a brief 20
727 KHz tone at 90dB SPL when held 30cm above the mouse. Contact Prof. K.P. Steel, MRC Institute
728 of Hearing Research, University Park, Nottingham NG7 2RD.
- 729 11. A ruler.
- 730 12. A 30 cm clear Plexiglas tube with an internal diameter of 2.5 cm for the contact righting reflex.

731 **4.5 Electrophysiology**

732 Preparation of acute cerebellar slices

733 Acute parasagittal slices of 300 μm thickness were prepared from the cerebellum of experimental and
734 control littermate mice by following published methods (Hansen et al., 2013). In brief, cerebella were
735 quickly removed and immersed in an ice-cold extracellular solution with composition of (mM): 119 NaCl,
736 26 NaHCO_3 , 11 glucose, 2.5 KCl, 2.5 CaCl_2 , 1.3 MgCl_2 and 1 NaH_2PO_4 , pH 7.4 when gassed with 5%
737 $\text{CO}_2/95\% \text{O}_2$. Cerebella were sectioned parasagittally using a vibratome (Leica VT-1000, Leica
738 Biosystems, Nussloch, Germany) and initially incubated at 35°C for ~30 min, and then equilibrated and
739 stored at room temperature until use.

740 Extracellular Electrophysiology

741 Extracellular and intracellular recordings were obtained from Purkinje neurons (PNs) in slices
742 constantly perfused with carbogen-bubbled extracellular solution and maintained at either 37° C
743 (extracellular) or 32° C (intracellular) $\pm 1^\circ \text{C}$ (see above). Cells were visualized with DIC optics and a
744 water-immersion 40x objective (NA 0.75) using a Zeiss Examiner microscope. Glass pipettes of ~3 $\text{M}\Omega$
745 resistance (Model P-1000, Sutter instruments, Novato, CA) were filled with either extracellular solution
746 and positioned near PN axon hillocks in order to measure action potential-associated capacitive current
747 transients in voltage clamp mode with the pipette potential held at 0 mV. For whole-cell patch clamp
748 recordings, pipettes were filled with an intracellular solution (mM): 140 KMeth ($\text{CH}_3\text{KO}_3\text{S}$), 10 NaCl, 2
749 MgCl_2 , 0.2 CaCl_2 , 10 HEPES, 14 Phosphocreatine (tris salt), 1 EGTA, 4 Mg-ATP, 0.4 Na-GTP. 100 μM
750 Picrotoxin (Sigma) was added to block inhibitory GABAergic synaptic inputs. Data was acquired using

Perez et al. Resubmission

751 a MultiClamp 700B amplifier at 20 or 100 kHz in voltage or current clamp mode, Digidata 1440 with
752 pClamp10 (Molecular Devices, Sunnyvale, CA) and filtered at 2 to 4 kHz. The series resistance was
753 usually between 10 and 15 M Ω . Series resistance was compensated at 80% for short term plasticity
754 experiments only.

755 For extracellular recordings, a total of 20 to 45 PNs were recorded from for each animal across all
756 genotypes, sexes, and age groups. Recordings were distributed across both the medial-lateral and
757 rostro-caudal axis of the cerebellum. Only cells with a “healthy” look (low contrast of cellular borders),
758 and regular, uninterrupted firing rate were examined. During analysis, a few cells were found to have
759 gaps in firing of greater than 2 second and these cells were eliminated from analysis, as this type of
760 firing is associated with being “unhealthy.” Double mutant tissue did not qualitatively differ in
761 appearance under DIC microscopy prior to recordings, nor was the number of “unhealthy” cells greater
762 than that of other genotypes (7% vs 4 to 11% of all cells across control genotypes at P400). Spatial
763 comparison of neural activity was obtained by recording from serial sections in the flocculus, lateral (2nd
764 or 3rd), intermediate (6th or 7th), and medial (11th or 12th) slices. Lower number slices were used in the
765 younger age groups (P45 and 110) to roughly match the relative positioning of recordings across age
766 groups. 0-3 recordings were made from each lobule within each slice dependent on tissue quality and
767 health. Each recording lasted for 1-minute. 3 to 5 mice were used for each age group and the
768 experimenter was blinded to the genotype, age, and sex.

769 Intracellular recordings were obtained from PNs in either folia III or VIII of the vermis, no statistical
770 differences in properties were observed between folia.

771 Analyses

772 Spontaneous action potential interstimulus intervals detected and analyzed using standard and custom
773 routines in ClampFit (Molecular Device), IgorPro (Wavemetrics), and Excel (Microsoft). Specifically,
774 action potentials were threshold detected and spiking statistics (i.e., frequency and interval length),
775 determined using adapted IgorPro routines (Taro Tools; <https://sites.google.com/site/tarotoolsregister/>).

Perez et al. Resubmission

776 The coefficient of variation of the mean inter-spike interval (CV) and the median inter-spike interval
777 ($CV = \frac{\sqrt{\sum (ISIn+1 - ISIn)^2}}{\sum (ISIn+1 + ISIn)}$) were calculated in Excel using custom macros.

778 Standard membrane properties were analyzed using IgorPro. R_M was determined by averaging 3
779 voltage trace responses to a -5 mV step pulse from a -80 mV holding potential and measuring the
780 resulting current deflection between 900 and 1000 ms after onset. The membrane time constant was
781 measured by fitting a single exponential to the initial decay phase from 90 to 10% of the peak. C_M was
782 calculated by dividing the membrane time constant by the R_M . mEPSC events were recorded over a 1-
783 minute epoch and detected and measured using Neuroexpress (v21.1.13). Parallel and climbing fiber
784 axons were stimulated using theta-glass electrodes (W.P.I.) and a TTL controlled stimulus isolator
785 (ISO-Flex, A.M.P.I.). Evoked EPSC amplitudes and decay time constants (1 exp. for parallel and 2 exp.
786 for climbing fibers) were analyzed using custom routines in IgorPro. Action potentials were examined as
787 part of a set of 1 s current injections between -500 and 2250 pA (250 pA steps) with a holding current
788 adjusted to maintain an ~70 mV potential. Action potential waveforms were measured using custom
789 routines in IgorPro. Action potential threshold was defined as the first membrane voltage in which the
790 first derivative exceeded 30 mV/ms (Zhu et al. 2006).

791 **4.6 Examination of Cerebellar Atrophy**

792 Cerebellar size

793 Immediately after brain removal from the skull, a dorsal, whole mount image was obtained. Images
794 were then processed using Fiji (NIH). The forebrain and cerebellar sizes were assessed by outlining
795 their 2-dimensional space and then calculating area. We normalized for possible differences in overall
796 brain size by dividing the results of the cerebellum by forebrain size to produce a relative cerebellum to
797 forebrain ratio. Experimenters were blind to the genotype of the animal.

798 Immunohistochemistry

799 At the respective study endpoints (P45, 120, 210, 400), male and female mice of all genotypes
800 represented in this study were anesthetized with isoflurane and underwent transcardial perfusion with

Perez et al. Resubmission

801 phosphate-buffered saline followed by 4% (w/v) buffered paraformaldehyde (PFA) and then dissected
802 to extract the brain. Images of the whole brain were taken immediately after removing the brain from
803 the skull and the brains were then submerged in 4% PFA for 24-hours, followed by 72-hours in 30%
804 sucrose in Tris-buffered saline (TBS) with 0.05% azide, and then cryoprotected in TBS-AF and stored
805 at 4°C until further use. The cerebellum was separated from the forebrain and parasagittally sectioned
806 using a sliding microtome (Microm HM 430, Thermo Scientific) set to section at 40 µm thickness.
807 Cerebellum sections were collected in a series of six and stored in TBS-AF at 4° C until further use. For
808 immunofluorescent visualization of Purkinje neurons, cerebellum sections of both *Atm*^{+/+}; *Aptx*^{+/+} and
809 *Atm*^{R35X/R35X}; *Aptx*^{-/-} (n = 5 per genotype) were washed for 5 min in TBS three times, and then blocked in
810 15% normal goat serum at room temperature for 30 min followed by free floating incubation in rabbit
811 anti-calbindin D-28k (1:1000) for 1 hour at room temperature on an orbital shaker, then washed for 5
812 min with TBS three times, followed by free floating incubation in goat anti-rabbit Alexa Fluor 488
813 (1:1000) for 1 h in the dark at room temperature on an orbital shaker. Following secondary antibody
814 incubation, sections were washed for 5 min in TBS three times and stored in TBS until further use.
815 Sections were mounted and cover-slipped with Fluoromount-G with DAPI. Slides were scanned using
816 Stereo Investigator version 2020.1.3 64bit (MBF Bioscience) on a Zeiss Axio Imager.M2 microscope
817 (Carl Zeiss Microscopy) using a 20x objective (NA 0.5) and images captured with a Hamamatsu ORCA
818 Flash 4.0 LT C11440 digital camera (Hamamatsu Photonics). To quantify the number of calbindin-
819 reactive cells in each folia in the resulting images, we randomly drew 2 lines between 300 to 500 µm
820 long in each folia and manually counted the total number of PNs along the length within the 40 µm
821 thickness of the tissue slice. 2D density (# of PNs/(linear length * 40 um thickness)) of the two samples
822 per folia were then averaged for further between folia and subject comparison. Experimenter was
823 blinded to mouse genotype.

824 Molecular (Calbindin) and granule cell (DAPI) layer widths were assessed by taking two width
825 measurements at two predefined locations for each folia, roughly halfway along the long extent of each

Perez et al. Resubmission

826 folia. Experimenter was blinded to the mouse genotype in which slices were examined and the order of
827 examination was interleaved.

828 **4.7 Flow Cytometry Measurements**

829 Flow cytometry analysis of blood and thymus cells was performed by staining with specific anti-mouse
830 antibodies: CD4, CD8, CD3, CD44, and CD25. Briefly, whole-blood samples (50 μ l) were stained using
831 fluorescent-labeled antibodies, then red-blood cells were lysed using BD lysing solution while live white-
832 blood cells were stained using a viability stain. Thymi were mechanically dissociated. 1 to 2 million
833 thymus cells were similarly stained using specific antibodies for CD4, CD8, CD44 and CD25. Analysis
834 of immuno-stained white blood cells or thymus samples was performed using FACS ARIA III and data
835 analyzed using FlowJo software as reported previously (Sanghez et al. 2017).

836 **4.8 Western Blots**

837 Protein extracts (cells/tissues) were homogenized in radioimmunoprecipitation assay (RIPA) lysis buffer
838 (150 mM NaCl, 1% Nonidet P-40 [NP-40], 0.5% deoxycholate, 0.1% SDS, 50 mM Tris, pH 8.0) with
839 protease inhibitors (10 μ g/ml AEBSF, 10 μ g/ml leupeptin, 5 μ g/ml pepstatin, 5 μ g/ml chymotrypsin, 10
840 μ g/ml aprotinin). The protein extracts were sonicated then pelleted by centrifugation at 13,000 rpm for
841 15 min at 4°C. BCA protein assay was used to quantify protein concentrations. Samples containing
842 equal amounts of protein 50 to 100 μ g per lane were separated using 4 to 12% gradient TGX precast
843 gels BioRad then transferred by TransBlot Semi-Dry BioRad system using Nitrocellulose transfer pack.
844 Transferred blots were stained by Ponceau S stain for equal protein loading then washed and blocked
845 with 5% nonfat dry milk in TBST for 60 min at room temp. Primary antibodies were incubated with
846 shaking overnight at 4°C. Blots were probed for the following antibodies: ATM (D2E2) Rabbit mAb Cell
847 Signaling, at 1:1000 dilution, β -Actin (D6A8) Rabbit mAb Cell Signaling, GAPDH (D16H11) Rabbit mAb
848 Cell Signaling followed by the appropriate horseradish peroxidase–conjugated (HRP) secondary Anti-
849 rabbit, Anti-mouse for 2 hours at room temperature. After multiple washes with TBST, Protein
850 expression was detected by Radiance Plus chemiluminescence substrate using the Azure c400 and the

Perez et al. Resubmission

851 BioRad ChemiDoc imaging systems. Densitometric analysis of the ATM was performed using ImageJ.
852 Experiments were performed with 2 technical and 2-3 biological replicates as indicated.

853 **4.9 Statistical Assessment**

854 The number of animals chosen for each group was based on a priori power analyses using GPower
855 v3.1 based on an α size of 0.5, power of 0.8, and effect sizes estimated from preliminary data or prior
856 studies. We used both parametric (1- and 2-way ANOVA) for normally distributed and non-parametric
857 (Kruskal Wallace) statistical methods for interval data to test for differences between groups followed by
858 pairwise multiple comparisons tests as indicated in the text. Outliers for immune data in Figs. 6 and 7
859 were excluded via the ROUT method (Q=2%). The specific analyses used for each data set is noted in
860 each figure legend. For all figures: * $p \leq 0.05$, ** $p < 0.01$, *** $p < 0.001$, **** $p < 0.0001$. Data are
861 reported as mean \pm SEM and box and whisker plots indicate the minimum, first quartile, median, third
862 quartile, and maximum data values. All figures and statistical analyses were completed using Excel
863 (Microsoft 360) or Prism v8 and 9 (Graphpad).

864 **5.0 Acknowledgements**

865 We would like to thank the UCLA Behavioral Core, especially Irina Zhuravka for her efforts assaying
866 behavioral deficits in the mice. We would also like to thank Dr. Jennifer Fogel for comments and edits to
867 the manuscript.

868 **6.0 Competing interests**

869 The authors declare that no competing interests exist.

870 **7.0 Citations**

871 Ady, Visou, Brenda Toscano-Márquez, Moushumi Nath, Philip K Chang, Jeanette Hui, Anna Cook,
872 François Charron, Roxanne Larivière, Bernard Brais, and R Anne McKinney. 2018. 'Altered
873 synaptic and firing properties of cerebellar Purkinje cells in a mouse model of ARSACS', *The*
874 *Journal of physiology*, 596: 4253-67.

Perez et al. Resubmission

- 875 Aguilar, M. J., S. Kamoshita, B. H. Landing, E. Boder, and R. P. Sedgwick. 1968a. 'Pathological
876 observations in ataxia-telangiectasia. A report of five cases', *Journal of Neuropathology and*
877 *Experimental Neurology*, 27: 659-76.
- 878 Aguilar, Mary Jane, Shigehiko Kamoshita, Benjamin H. Landing, Elena Boder, and Robert P. Sedgwick.
879 1968b. 'Pathological Observations in Ataxia-Telangiectasia: A Report on Five Cases*', *Journal*
880 *of Neuropathology and Experimental Neurology*, 27: 659-76.
- 881 Ahel, I., U. Rass, S. F. El-Khamisy, S. Katyal, P. M. Clements, P. J. McKinnon, K. W. Caldecott, and S.
882 C. West. 2006. 'The neurodegenerative disease protein aprataxin resolves abortive DNA
883 ligation intermediates', *Nature*, 443: 713-6.
- 884 Aicardi, J., C. Barbosa, E. Andermann, F. Andermann, R. Morcos, Q. Ghanem, Y. Fukuyama, Y.
885 Awaya, and P. Moe. 1988. 'Ataxia-ocular motor apraxia: a syndrome mimicking ataxia-
886 telangiectasia', *Annals of Neurology*, 24: 497-502.
- 887 Alviña, Karina, and Kamran Khodakhah. 2010. 'KCa channels as therapeutic targets in episodic ataxia
888 type-2', *Journal of Neuroscience*, 30: 7249-57.
- 889 Amromin, George D, Elena Boder, and Raymond Teplitz. 1979. 'Ataxia-telangiectasia with a 32 year
890 survival: a clinicopathological report', *Journal of Neuropathology and Experimental Neurology*,
891 38: 621-43.
- 892 Ando, K., J. L. Kernan, P. H. Liu, T. Sanda, E. Logette, J. Tschopp, A. T. Look, J. Wang, L. Bouchier-
893 Hayes, and S. Sidi. 2012. 'PIDD death-domain phosphorylation by ATM controls prodeath
894 versus prosurvival PIDDosome signaling', *Molecular Cell*, 47: 681-93.
- 895 Apps, R., and R. Hawkes. 2009. 'Cerebellar cortical organization: a one-map hypothesis', *Nature*
896 *Reviews: Neuroscience*, 10: 670-81.
- 897 Atluri, Pradeep P., and Wade G. Regehr. 1996. 'Determinants of the Time Course of Facilitation at the
898 Granule Cell to Purkinje Cell Synapse', *The Journal of Neuroscience*, 16: 5661-71.
- 899 Barlow, C., S. Hirotsune, R. Paylor, M. Liyanage, M. Eckhaus, F. Collins, Y. Shiloh, J. N. Crawley, T.
900 Ried, D. Tagle, and A. Wynshaw-Boris. 1996. 'Atm-deficient mice: a paradigm of ataxia
901 telangiectasia', *Cell*, 86: 159-71.
- 902 Beraldi, R., D. K. Meyerholz, A. Savinov, A. D. Kovacs, J. M. Weimer, J. A. Dykstra, R. D. Geraets, and
903 D. A. Pearce. 2017. 'Genetic ataxia telangiectasia porcine model phenocopies the multisystemic
904 features of the human disease', *Biochim Biophys Acta Mol Basis Dis*, 1863: 2862-70.
- 905 Bhatt, Jayesh M., and Andrew Bush. 2014. 'Microbiological surveillance in lung disease in ataxia
906 telangiectasia', *European Respiratory Journal*, 43: 1797-801.
- 907 Boder, Elena, and Robert P. Sedgwick. 1958. 'ATAXIA-TELANGIECTASIA', *A Familial Syndrome of*
908 *Progressive Cerebellar Ataxia, Oculocutaneous Telangiectasia and Frequent Pulmonary*
909 *Infection*, 21: 526-54.
- 910 Bogue, M. A., C. Wang, C. Zhu, and D. B. Roth. 1997. 'V(D)J recombination in Ku86-deficient mice:
911 distinct effects on coding, signal, and hybrid joint formation', *Immunity*, 7: 37-47.
- 912 Bosch, Marie K, Yarimar Carrasquillo, Joseph L Ransdell, Ajay Kanakamedala, David M Ornitz, and
913 Jeanne M Nerbonne. 2015. 'Intracellular FGF14 (iFGF14) is required for spontaneous and
914 evoked firing in cerebellar Purkinje neurons and for motor coordination and balance', *Journal of*
915 *Neuroscience*, 35: 6752-69.
- 916 Bradley, A., K. Anastassiadis, A. Ayadi, J. F. Battey, C. Bell, M. C. Birling, J. Bottomley, S. D. Brown, A.
917 Bürger, C. J. Bult, W. Bushell, F. S. Collins, C. Desaintes, B. Doe, A. Economides, J. T. Eppig,
918 R. H. Finnell, C. Fletcher, M. Fray, D. Friendewey, R. H. Friedel, F. G. Grosveld, J. Hansen, Y.
919 Hérault, G. Hicks, A. Hörlein, R. Houghton, M. Hrabé de Angelis, D. Huylebroeck, V. Iyer, P. J.
920 de Jong, J. A. Kadin, C. Kaloff, K. Kennedy, M. Koutsourakis, K. C. Lloyd, S. Marschall, J.
921 Mason, C. McKerlie, M. P. McLeod, H. von Melchner, M. Moore, A. O. Mujica, A. Nagy, M.
922 Nefedov, L. M. Nutter, G. Pavlovic, J. L. Peterson, J. Pollock, R. Ramirez-Solis, D. E. Rancourt,
923 M. Raspa, J. E. Remacle, M. Ringwald, B. Rosen, N. Rosenthal, J. Rossant, P. Ruiz Noppinger,
924 E. Ryder, J. Z. Schick, F. Schnütgen, P. Schofield, C. Seisenberger, M. Selloum, E. M.
925 Simpson, W. C. Skarnes, D. Smedley, W. L. Stanford, A. F. Stewart, K. Stone, K. Swan, H.
926 Tadepally, L. Teboul, G. P. Tocchini-Valentini, D. Valenzuela, A. P. West, K. Yamamura, Y.

Perez et al. Resubmission

- 927 Yoshinaga, and W. Wurst. 2012. 'The mammalian gene function resource: the International
928 Knockout Mouse Consortium', *Mammalian Genome*, 23: 580-6.
- 929 Bredemeyer, Andrea L, Girdhar G Sharma, Ching-Yu Huang, Beth A Helmsink, Laura M Walker, Katrina
930 C Khor, Beth Nuskey, Kathleen E Sullivan, Tej K Pandita, and Craig H Bassing. 2006. 'ATM
931 stabilizes DNA double-strand-break complexes during V (D) J recombination', *Nature*, 442: 466-
932 70.
- 933 Browne, Susan E., L. Jackson Roberts, Phyllis A. Dennery, Susan R. Doctrow, M. Flint Beal, Carrolee
934 Barlow, and Rodney L. Levine. 2004. 'Treatment with a catalytic antioxidant corrects the
935 neurobehavioral defect in ataxia-telangiectasia mice', *Free Radical Biology and Medicine*, 36:
936 938-42.
- 937 Çaglayan, Melike, Rajendra Prasad, Rachel Krasich, Matthew J. Longley, Kei Kadoda, Masataka
938 Tsuda, Hiroyuki Sasanuma, Shunichi Takeda, Keizo Tano, William C. Copeland, and Samuel H.
939 Wilson. 2017. 'Complementation of aprataxin deficiency by base excision repair enzymes in
940 mitochondrial extracts', *Nucleic Acids Research*, 45: 10079-88.
- 941 Campbell, A., B. Krupp, J. Bushman, M. Noble, C. Pröschel, and M. Mayer-Pröschel. 2015. 'A novel
942 mouse model for ataxia-telangiectasia with a N-terminal mutation displays a behavioral defect
943 and a low incidence of lymphoma but no increased oxidative burden', *Human Molecular
944 Genetics*, 24: 6331-49.
- 945 Campbell, Andrew, Jared Bushman, Joshua Munger, Mark Noble, Christoph Pröschel, and Margot
946 Mayer-Pröschel. 2016. 'Mutation of ataxia-telangiectasia mutated is associated with
947 dysfunctional glutathione homeostasis in cerebellar astroglia', *Glia*, 64: 227-39.
- 948 Chao, Connie, Eva Marie Yang, and Yang Xu. 2000. 'Rescue of Defective T Cell Development and
949 Function in *Atm*^{-/-} Mice by a Functional TCR $\alpha\beta$ Transgene', *The Journal of Immunology*, 164:
950 345-49.
- 951 Chatterjee, Nimrat, and Graham C. Walker. 2017. 'Mechanisms of DNA damage, repair, and
952 mutagenesis', *Environmental and Molecular Mutagenesis*, 58: 235-63.
- 953 Chen, Philip, Cheng Peng, John Luff, Kevin Spring, Dianne Watters, Steven Bottle, Shigeki Furuya, and
954 Martin F. Lavin. 2003. 'Oxidative Stress Is Responsible for Deficient Survival and
955 Dendritogenesis in Purkinje Neurons from Ataxia-Telangiectasia Mutated Mutant Mice', *The
956 Journal of Neuroscience*, 23: 11453-60.
- 957 Chen, Xi, Tie-Shan Tang, Huiping Tu, Omar Nelson, Mark Pook, Robert Hammer, Nobuyuki Nukina,
958 and Ilya Bezprozvanny. 2008. 'Deranged calcium signaling and neurodegeneration in
959 spinocerebellar ataxia type 3', *Journal of Neuroscience*, 28: 12713-24.
- 960 Chou, W. C., L. Y. Hu, C. N. Hsiung, and C. Y. Shen. 2015. 'Initiation of the ATM-Chk2 DNA damage
961 response through the base excision repair pathway', *Carcinogenesis*, 36: 832-40.
- 962 Clark, H Brent, Eric N Burright, Wael S Yunis, Seth Larson, Claire Wilcox, Boyd Hartman, Antoni
963 Matilla, Huda Y Zoghbi, and Harry T Orr. 1997. 'Purkinje Cell Expression of a Mutant Allele of
964 SCA1 in Transgenic Mice Leads to Disparate Effects on Motor Behaviors, Followed by a
965 Progressive Cerebellar Dysfunction and Histological Alterations', *Journal of Neuroscience*, 17:
966 7385-95.
- 967 Clements, P. M., C. Breslin, E. D. Deeks, P. J. Byrd, L. Ju, P. Bieganowski, C. Brenner, M. C. Moreira,
968 A. M. Taylor, and K. W. Caldecott. 2004. 'The ataxia-oculomotor apraxia 1 gene product has a
969 role distinct from ATM and interacts with the DNA strand break repair proteins XRCC1 and
970 XRCC4', *DNA Repair (Amst)*, 3: 1493-502.
- 971 Concannon, P., and R. A. Gatti. 1997. 'Diversity of ATM gene mutations detected in patients with
972 ataxia-telangiectasia', *Human Mutation*, 10: 100-7.
- 973 Cook, Anna A., Eviatar Fields, and Alanna J. Watt. 2020. 'Losing the Beat: Contribution of Purkinje Cell
974 Firing Dysfunction to Disease, and Its Reversal', *Neuroscience*.
- 975 Coutinho P, Barbot C, Coutinho P. 2002. 'Ataxia with Oculomotor Apraxia Type 1.' in Ardinger HH
976 Adam MP, Pagon RA, et al. (ed.), *GeneReviews*® (GeneReviews® [Internet]: University of
977 Washington, Seattle).
- 978 Crawford, T. O., R. L. Skolasky, R. Fernandez, K. J. Rosquist, and H. M. Lederman. 2006. 'Survival
979 probability in ataxia telangiectasia', *Archives of Disease in Childhood*, 91: 610-11.

Perez et al. Resubmission

- 980 De Leon, G. A., W. D. Grover, and D. S. Huff. 1976. 'Neuropathologic changes in ataxia-telangiectasia',
981 *Neurology*, 26: 947-51.
- 982 Dell'Orco, James M., Aaron H. Wasserman, Ravi Chopra, Melissa A. C. Ingram, Yuan-Shih Hu, Vikrant
983 Singh, Heike Wulff, Puneet Opal, Harry T. Orr, and Vikram G. Shakkottai. 2015. 'Neuronal
984 Atrophy Early in Degenerative Ataxia Is a Compensatory Mechanism to Regulate Membrane
985 Excitability', *The Journal of Neuroscience*, 35: 11292-307.
- 986 Dell'Orco, James M, Stefan M Pulst, and Vikram G Shakkottai. 2017. 'Potassium channel dysfunction
987 underlies Purkinje neuron spiking abnormalities in spinocerebellar ataxia type 2', *Human
988 Molecular Genetics*, 26: 3935-45.
- 989 Demaerel, PH, BE Kendall, and D Kingsley. 1992. 'Cranial CT and MRI in diseases with DNA repair
990 defects', *Neuroradiology*, 34: 117-21.
- 991 Dineen, Rob A., Felix Raschke, Hannah L. McGlashan, Stefan Pszczolkowski, Lorna Hack, Andrew D.
992 Cooper, Manish Prasad, Gabriel Chow, William P. Whitehouse, and Dorothee P. Auer. 2020.
993 'Multiparametric cerebellar imaging and clinical phenotype in childhood ataxia telangiectasia',
994 *NeuroImage: Clinical*, 25: 102110.
- 995 Du, L., M. E. Jung, R. Damoiseaux, G. Completo, F. Fike, J. M. Ku, S. Nahas, C. Piao, H. Hu, and R. A.
996 Gatti. 2013. 'A new series of small molecular weight compounds induce read through of all three
997 types of nonsense mutations in the ATM gene', *Molecular Therapy*, 21: 1653-60.
- 998 El-Brolosy, Mohamed A., and Didier Y. R. Stainier. 2017. 'Genetic compensation: A phenomenon in
999 search of mechanisms', *Plos Genetics*, 13: e1006780-e80.
- 1000 Elson, A., Y. Wang, C. J. Daugherty, C. C. Morton, F. Zhou, J. Campos-Torres, and P. Leder. 1996.
1001 'Pleiotropic defects in ataxia-telangiectasia protein-deficient mice', *Proceedings of the National
1002 Academy of Sciences of the United States of America*, 93: 13084-9.
- 1003 Gao, Zhenyu, Boeke J van Beugen, and Chris I De Zeeuw. 2012. 'Distributed synergistic plasticity and
1004 cerebellar learning', *Nature Reviews: Neuroscience*, 13: 619-35.
- 1005 Gatti, R. A., and H. V. Vinters. 1985. 'Cerebellar pathology in ataxia-telangiectasia: the significance of
1006 basket cells', *Kroc Foundation Series*, 19: 225-32.
- 1007 Genik, P. C., H. Bielefeldt-Ohmann, X. Liu, M. D. Story, L. Ding, J. M. Bush, C. M. Fallgren, and M. M.
1008 Weil. 2014. 'Strain background determines lymphoma incidence in Atm knockout mice',
1009 *Neoplasia*, 16: 129-36.
- 1010 Germain, Ronald N. 2002. 'T-cell development and the CD4-CD8 lineage decision', *Nature Reviews
1011 Immunology*, 2: 309-22.
- 1012 Gertsenstein, Marina, Lauryl M. J. Nutter, Tammy Reid, Monica Pereira, William L. Stanford, Janet
1013 Rossant, and Andras Nagy. 2010. 'Efficient Generation of Germ Line Transmitting Chimeras
1014 from C57BL/6N ES Cells by Aggregation with Outbred Host Embryos', *PloS One*, 5: e11260.
- 1015 Gilad, Shlomit, Rami Khosravi, Dganit Shkedy, Tamar Uziel, Yael Ziv, Kinneret Savitsky, Galit Rotman,
1016 Sara Smith, Luciana Chessa, Timothy J. Jorgensen, Reli Harnik, Moshe Frydman, Ozden
1017 Sanal, Sima Portnoi, Zipora Goldwicz, N. G. J. Jaspers, Richard A. Gatti, Gilbert Lenoir, Martin
1018 F. Lavin, Kouichi Tatsumi, Rolf D. Wegner, Yosef Shiloh, and Anat Bar-Shira. 1996.
1019 'Predominance of Null Mutations in Ataxia-Telangiectasia', *Human Molecular Genetics*, 5: 433-
1020 39.
- 1021 Gueven, N., O. J. Becherel, A. W. Kijas, P. Chen, O. Howe, J. H. Rudolph, R. Gatti, H. Date, O.
1022 Onodera, G. Taucher-Scholz, and M. F. Lavin. 2004. 'Aprataxin, a novel protein that protects
1023 against genotoxic stress', *Human Molecular Genetics*, 13: 1081-93.
- 1024 Guo, Zhi, Sergei Kozlov, Martin F. Lavin, Maria D. Person, and Tanya T. Paull. 2010. 'ATM Activation
1025 by Oxidative Stress', *Science*, 330: 517-21.
- 1026 Hansel, Christian, and David J. Linden. 2000. 'Long-Term Depression of the Cerebellar Climbing Fiber-
1027 Purkinje Neuron Synapse', *Neuron*, 26: 473-82.
- 1028 Hansen, Stephen T, Pratap Meera, Thomas S Otis, and Stefan M Pulst. 2013. 'Changes in Purkinje cell
1029 firing and gene expression precede behavioral pathology in a mouse model of SCA2', *Human
1030 Molecular Genetics*, 22: 271-83.

Perez et al. Resubmission

- 1031 Hathcock, K. S., S. Bowen, F. Livak, and R. J. Hodes. 2013. 'ATM influences the efficiency of TCRbeta
1032 rearrangement, subsequent TCRbeta-dependent T cell development, and generation of the pre-
1033 selection TCRbeta CDR3 repertoire', *PloS One*, 8: e62188.
- 1034 Herzog, Karl-Heinz, Miriam J. Chong, Manuela Kapsetaki, James I. Morgan, and Peter J. McKinnon.
1035 1998. 'Requirement for Atm in Ionizing Radiation-Induced Cell Death in the Developing Central
1036 Nervous System', *Science*, 280: 1089-91.
- 1037 Hoche, F., K. Seidel, M. Theis, S. Vlaho, R. Schubert, S. Zielen, and M. Kieslich. 2012.
1038 'Neurodegeneration in ataxia telangiectasia: what is new? What is evident?', *Neuropediatrics*,
1039 43: 119-29.
- 1040 Hourez, Raphael, Laurent Servais, David Orduz, David Gall, Isabelle Millard, Alban de Kerchove
1041 d'Exaerde, Guy Cheron, Harry T Orr, Massimo Pandolfo, and Serge N Schiffmann. 2011.
1042 'Aminopyridines correct early dysfunction and delay neurodegeneration in a mouse model of
1043 spinocerebellar ataxia type 1', *Journal of Neuroscience*, 31: 11795-807.
- 1044 Hoxha, Eriola, Ilaria Balbo, Maria Concetta Miniaci, and Filippo Tempia. 2018. 'Purkinje Cell Signaling
1045 Deficits in Animal Models of Ataxia', *Frontiers in Synaptic Neuroscience*, 10: 6-6.
- 1046 Hurlock, Edward C, Anne McMahon, and Rolf H Joho. 2008. 'Purkinje-cell-restricted restoration of Kv3.
1047 3 function restores complex spikes and rescues motor coordination in Kcnc3 mutants', *Journal
1048 of Neuroscience*, 28: 4640-48.
- 1049 Jackson, Thomas J, Gabriel Chow, Mohnish Suri, Philip Byrd, Malcolm R Taylor, and William P
1050 Whitehouse. 2016. 'Longitudinal analysis of the neurological features of ataxia-telangiectasia',
1051 *Developmental Medicine and Child Neurology*, 58: 690-97.
- 1052 Jayabal, Sriram, Hui Ho Vanessa Chang, Kathleen E Cullen, and Alanna J Watt. 2016. '4-
1053 aminopyridine reverses ataxia and cerebellar firing deficiency in a mouse model of
1054 spinocerebellar ataxia type 6', *Scientific Reports*, 6: 1-12.
- 1055 Kaminsky, Natalie, Ofer Bihari, Sivan Kanner, and Ari Barzilai. 2016. 'Connecting Malfunctioning Glial
1056 Cells and Brain Degenerative Disorders', *Genomics, Proteomics & Bioinformatics*, 14: 155-65.
- 1057 Kano, Masanobu, and Takaki Watanabe. 2017. 'Type-1 metabotropic glutamate receptor signaling in
1058 cerebellar Purkinje cells in health and disease', *F1000Research*, 6: 416-16.
- 1059 Kastan, M. B., and J. Bartek. 2004. 'Cell-cycle checkpoints and cancer', *Nature*, 432: 316-23.
- 1060 Kasumu, Adebimpe, and Ilya Bezprozvanny. 2012. 'Deranged calcium signaling in Purkinje cells and
1061 pathogenesis in spinocerebellar ataxia 2 (SCA2) and other ataxias', *The Cerebellum*, 11: 630-
1062 39.
- 1063 Kim, Jusik, Keeun Kim, Jung-Soon Mo, and Youngsoo Lee. 2020. 'Atm deficiency in the DNA
1064 polymerase β null cerebellum results in cerebellar ataxia and Itpr1 reduction associated with
1065 alteration of cytosine methylation', *Nucleic Acids Research*, 48: 3678-91.
- 1066 Krangel, Michael S. 2009. 'Mechanics of T cell receptor gene rearrangement', *Current Opinion in
1067 Immunology*, 21: 133-39.
- 1068 Larivière, Roxanne, Nicolas Sgarioto, Brenda Toscano Márquez, Rébecca Gaudet, Karine Choquet, R
1069 Anne McKinney, Alanna J Watt, and Bernard Brais. 2019. 'Sacs R272C missense homozygous
1070 mice develop an ataxia phenotype', *Molecular Brain*, 12: 1-15.
- 1071 Lavin, M. F. 2013. 'The appropriateness of the mouse model for ataxia-telangiectasia: neurological
1072 defects but no neurodegeneration', *DNA Repair (Amst)*, 12: 612-9.
- 1073 Levy, Ariel, and Anthony E. Lang. 2018. 'Ataxia-telangiectasia: A review of movement disorders, clinical
1074 features, and genotype correlations', *Movement Disorders*, 33: 1238-47.
- 1075 Li, J., Y. R. Han, M. R. Plummer, and K. Herrup. 2009. 'Cytoplasmic ATM in neurons modulates
1076 synaptic function', *Current Biology*, 19: 2091-6.
- 1077 Li, Jiali, Jianmin Chen, Harry V. Vinters, Richard A. Gatti, and Karl Herrup. 2011. 'Stable Brain
1078 ATM Message and Residual Kinase-Active ATM Protein in Ataxia-Telangiectasia',
1079 *The Journal of Neuroscience*, 31: 7568-77.
- 1080 Lindahl, T., and D. E. Barnes. 2000. 'Repair of endogenous DNA damage', *Cold Spring Harbor
1081 Symposia on Quantitative Biology*, 65: 127-33.

Perez et al. Resubmission

- 1082 Liu, Jing, Tie-Shan Tang, Huiping Tu, Omar Nelson, Emily Herndon, Duong P Huynh, Stefan M Pulst,
1083 and Ilya Bezprozvanny. 2009. 'Deranged calcium signaling and neurodegeneration in
1084 spinocerebellar ataxia type 2', *Journal of Neuroscience*, 29: 9148-62.
- 1085 Livák, Ferenc, Michelle Tourigny, David G. Schatz, and Howard T. Petrie. 1999. 'Characterization of
1086 TCR Gene Rearrangements During Adult Murine T Cell Development', *The Journal of*
1087 *Immunology*, 162: 2575-80.
- 1088 Lorenzetti, Diego, Kei Watase, Bisong Xu, Martin M Matzuk, Harry T Orr, and Huda Y Zoghbi. 2000.
1089 'Repeat instability and motor incoordination in mice with a targeted expanded CAG repeat in the
1090 Sca1 locus', *Human Molecular Genetics*, 9: 779-85.
- 1091 Marshall, Jean S., Richard Warrington, Wade Watson, and Harold L. Kim. 2018. 'An introduction to
1092 immunology and immunopathology', *Allergy, asthma, and clinical immunology : official journal of*
1093 *the Canadian Society of Allergy and Clinical Immunology*, 14: 49-49.
- 1094 Matei, I. R., C. J. Guidos, and J. S. Danska. 2006. 'ATM-dependent DNA damage surveillance in T-cell
1095 development and leukemogenesis: the DSB connection', *Immunological Reviews*, 209: 142-58.
- 1096 Matsuoka, Shuhei, Bryan A. Ballif, Agata Smogorzewska, E. Robert McDonald, Kristen E. Hurov, Ji
1097 Luo, Corey E. Bakalarski, Zhenming Zhao, Nicole Solimini, Yaniv Lerenthal, Yosef Shiloh,
1098 Steven P. Gygi, and Stephen J. Elledge. 2007. 'ATM and ATR Substrate Analysis Reveals
1099 Extensive Protein Networks Responsive to DNA Damage', *Science*, 316: 1160-66.
- 1100 McKinnon, P. J. 2009. 'DNA repair deficiency and neurological disease', *Nature Reviews:*
1101 *Neuroscience*, 10: 100-12.
- 1102 Meagher, M., and R. N. Lightowlers. 2014. 'The role of TDP1 and APTX in mitochondrial DNA repair',
1103 *Biochimie*, 100: 121-4.
- 1104 Micol, R., L. Ben Slama, F. Suarez, L. Le Mignot, J. Beauté, N. Mahlaoui, C. Dubois d'Enghien, A.
1105 Laugé, J. Hall, J. Couturier, L. Vallée, B. Delobel, F. Rivier, K. Nguyen, T. Billette de Villemeur,
1106 J. L. Stephan, P. Bordigoni, Y. Bertrand, N. Aladjidi, J. M. Pedespan, C. Thomas, I. Pellier, M.
1107 Koenig, O. Hermine, C. Picard, D. Moshous, B. Neven, F. Lanternier, S. Blanche, M. Tardieu,
1108 M. Debré, A. Fischer, and D. Stoppa-Lyonnet. 2011. 'Morbidity and mortality from ataxia-
1109 telangiectasia are associated with ATM genotype', *Journal of Allergy and Clinical Immunology*,
1110 128: 382-9.e1.
- 1111 Monaco, S., E. Nardelli, G. Moretto, T. Cavallaro, and N. Rizzuto. 1988. 'Cytoskeletal pathology in
1112 ataxia-telangiectasia', *Clinical Neuropathology*, 7: 44-6.
- 1113 Moreira, M. C., S. Klur, M. Watanabe, A. H. Németh, I. Le Ber, J. C. Moniz, C. Tranchant, P. Aubourg,
1114 M. Tazir, L. Schöls, M. Pandolfo, J. B. Schulz, J. Pouget, P. Calvas, M. Shizuka-Ikeda, M. Shoji,
1115 M. Tanaka, L. Izatt, C. E. Shaw, A. M'Zahem, E. Dunne, P. Bomont, T. Benhassine, N.
1116 Bouslam, G. Stevanin, A. Brice, J. Guimarães, P. Mendonça, C. Barbot, P. Coutinho, J.
1117 Sequeiros, A. Dürr, J. M. Warter, and M. Koenig. 2004. 'Senataxin, the ortholog of a yeast RNA
1118 helicase, is mutant in ataxia-ocular apraxia 2', *Nature Genetics*, 36: 225-7.
- 1119 Morrell, Daphne, Elizabeth Cromartie, and Michael Swift. 1986. 'Mortality and cancer incidence in 263
1120 patients with ataxia-telangiectasia', *Journal of the National Cancer Institute*, 77: 89-92.
- 1121 Paula-Barbosa, M. M., C. Ruela, M. A. Tavares, C. Pontes, A. Saraiva, and C. Cruz. 1983. 'Cerebellar
1122 cortex ultrastructure in ataxia-telangiectasia', *Annals of Neurology*, 13: 297-302.
- 1123 Perkins, Emma M, Yvonne L Clarkson, Nancy Sabatier, David M Longhurst, Christopher P Millward,
1124 Jennifer Jack, Junko Toraiwa, Mitsunori Watanabe, Jeffrey D Rothstein, and Alastair R Lyndon.
1125 2010. 'Loss of β -III spectrin leads to Purkinje cell dysfunction recapitulating the behavior and
1126 neuropathology of spinocerebellar ataxia type 5 in humans', *Journal of Neuroscience*, 30: 4857-
1127 67.
- 1128 Petersen, Andrew J., Stacey A. Rimkus, and David A. Wassarman. 2012. 'ATM kinase inhibition in glial
1129 cells activates the innate immune response and causes neurodegeneration in
1130 *Drosophila*', *Proceedings of the National Academy of Sciences*, 109: E656-E64.
- 1131 Pizzamiglio, L., E. Focchi, and F. Antonucci. 2020. 'ATM Protein Kinase: Old and New Implications in
1132 Neuronal Pathways and Brain Circuitry', *Cells*, 9.
- 1133 Quarantelli, Mario, Giuliana Giardino, Anna Prinster, Giuseppina Aloj, Barbara Carotenuto, Emilia
1134 Cirillo, Angela Marsili, Elena Salvatore, Ennio Del Giudice, and Claudio Pignata. 2013. 'Steroid

Perez et al. Resubmission

- 1135 treatment in Ataxia-Telangiectasia induces alterations of functional magnetic resonance imaging
1136 during pronosupination task', *European Journal of Paediatric Neurology*, 17: 135-40.
- 1137 Quek, Hazel, John Luff, KaGeen Cheung, Sergei Kozlov, Magtoug Gatei, C. Soon Lee, Mark C.
1138 Bellingham, Peter G. Noakes, Yi Chieh Lim, Nigel L. Barnett, Steven Dingwall, Ernst Wolvetang,
1139 Tomoji Mashimo, Tara L. Roberts, and Martin F. Lavin. 2016. 'A rat model of ataxia-
1140 telangiectasia: evidence for a neurodegenerative phenotype', *Human Molecular Genetics*, 26:
1141 109-23.
- 1142 Rashi-Elkeles, S., R. Elkon, N. Weizman, C. Linhart, N. Amariglio, G. Sternberg, G. Rechavi, A.
1143 Barzilai, R. Shamir, and Y. Shiloh. 2006. 'Parallel induction of ATM-dependent pro- and
1144 antiapoptotic signals in response to ionizing radiation in murine lymphoid tissue', *Oncogene*, 25:
1145 1584-92.
- 1146 Rass, Ulrich, Ivan Ahel, and Stephen C. West. 2007. 'Defective DNA Repair and Neurodegenerative
1147 Disease', *Cell*, 130: 991-1004.
- 1148 Rogers, D. C., E. M. Fisher, S. D. Brown, J. Peters, A. J. Hunter, and J. E. Martin. 1997. 'Behavioral
1149 and functional analysis of mouse phenotype: SHIRPA, a proposed protocol for comprehensive
1150 phenotype assessment', *Mammalian Genome*, 8: 711-3.
- 1151 Rothblum-Oviatt, Cynthia, Jennifer Wright, Maureen A. Lefton-Greif, Sharon A. McGrath-Morrow,
1152 Thomas O. Crawford, and Howard M. Lederman. 2016. 'Ataxia telangiectasia: a review',
1153 *Orphanet Journal of Rare Diseases*, 11: 159.
- 1154 Sahama, Ishani, Kate Sinclair, Simona Fiori, James Doecke, Kerstin Pannek, Lee Reid, Martin Lavin,
1155 and Stephen Rose. 2015. 'Motor pathway degeneration in young ataxia telangiectasia patients:
1156 A diffusion tractography study', *NeuroImage: Clinical*, 9: 206-15.
- 1157 Sahama, Ishani, Kate Sinclair, Kerstin Pannek, Martin Lavin, and Stephen Rose. 2014. 'Radiological
1158 imaging in ataxia telangiectasia: a review', *The Cerebellum*, 13: 521-30.
- 1159 Sandoval, N., M. Platzer, A. Rosenthal, T. Dork, R. Bendix, B. Skawran, M. Stuhmann, R. D. Wegner,
1160 K. Sperling, S. Banin, Y. Shiloh, A. Baumer, U. Bernthaler, H. Sennefelder, M. Brohm, B. H.
1161 Weber, and D. Schindler. 1999. 'Characterization of ATM gene mutations in 66 ataxia
1162 telangiectasia families', *Human Molecular Genetics*, 8: 69-79.
- 1163 Sanghez, Valentina, Anna Luzzi, Don Clarke, Dustin Kee, Steven Beuder, Danielle Rux, Mitsujiro
1164 Osawa, Joaquín Madrenas, Tsui-Fen Chou, Michael Kyba, and Michelina Iacovino. 2017.
1165 'Notch activation is required for downregulation of HoxA3-dependent endothelial cell phenotype
1166 during blood formation', *PLoS One*, 12: e0186818.
- 1167 Savitsky, K., A. Bar-Shira, S. Gilad, G. Rotman, Y. Ziv, L. Vanagaite, D. A. Tagle, S. Smith, T. Uziel, S.
1168 Sfez, M. Ashkenazi, I. Pecker, M. Frydman, R. Harnik, S. R. Patanjali, A. Simmons, G. A.
1169 Clines, A. Sartiel, R. A. Gatti, L. Chessa, O. Sanal, M. F. Lavin, N. G. Jaspers, A. M. Taylor, C.
1170 F. Arlett, T. Miki, S. M. Weissman, M. Lovett, F. S. Collins, and Y. Shiloh. 1995. 'A single ataxia
1171 telangiectasia gene with a product similar to PI-3 kinase', *Science*, 268: 1749-53.
- 1172 Schellenberg, M. J., P. P. Tumbale, and R. S. Williams. 2015. 'Molecular underpinnings of Aprataxin
1173 RNA/DNA deadenylase function and dysfunction in neurological disease', *Progress in
1174 Biophysics and Molecular Biology*, 117: 157-65.
- 1175 Schubert, R., J. Reichenbach, and S. Zielen. 2002. 'Deficiencies in CD4+ and CD8+ T cell subsets in
1176 ataxia telangiectasia', *Clinical and Experimental Immunology*, 129: 125-32.
- 1177 Sedghi, Maryam, Mehri Salari, Ali-Reza Moslemi, Ariana Kariminejad, Mark Davis, Hayley Goullée,
1178 Björn Olsson, Nigel Laing, and Homa Tajsharghi. 2018. 'Ataxia-telangiectasia-like disorder in a
1179 family deficient for MRE11A, caused by a MRE11 variant', *Neurology Genetics*, 4:
1180 e295.
- 1181 Shakkottai, Vikram G, Maria do Carmo Costa, James M Dell'Orco, Ananthkrishnan
1182 Sankaranarayanan, Heike Wulff, and Henry L Paulson. 2011a. 'Early changes in cerebellar
1183 physiology accompany motor dysfunction in the polyglutamine disease spinocerebellar ataxia
1184 type 3', *Journal of Neuroscience*, 31: 13002-14.
- 1185 Shakkottai, Vikram G, Maolei Xiao, Lin Xu, Michael Wong, Jeanne M Nerbonne, David M Ornitz, and
1186 Kelvin A Yamada. 2009. 'FGF14 regulates the intrinsic excitability of cerebellar Purkinje
1187 neurons', *Neurobiology of Disease*, 33: 81-88.

Perez et al. Resubmission

- 1188 Shakkottai, Vikram G., Maria do Carmo Costa, James M. Dell'Orco, Ananthkrishnan
1189 Sankaranarayanan, Heike Wulff, and Henry L. Paulson. 2011b. 'Early Changes in Cerebellar
1190 Physiology Accompany Motor Dysfunction in the Polyglutamine Disease Spinocerebellar Ataxia
1191 Type 3', *The Journal of Neuroscience*, 31: 13002-14.
- 1192 Shiloh, Yosef. 2020. 'The cerebellar degeneration in ataxia-telangiectasia: A case for genome
1193 instability', *DNA Repair*, 95: 102950.
- 1194 Shiloh, Yosef, and Yael Ziv. 2013. 'The ATM protein kinase: regulating the cellular response to
1195 genotoxic stress, and more', *Nature Reviews Molecular Cell Biology*, 14: 197-210.
- 1196 Solitare, G. B. 1968. 'Louis-Bar's syndrome (ataxia-telangiectasia). Anatomic considerations with
1197 emphasis on neuropathologic observations', *Neurology*, 18: 1180-6.
- 1198 Solitare, G. B., and V. F. Lopez. 1967. 'Louis-bar's syndrome (ataxia-telangiectasia). Neuropathologic
1199 observations', *Neurology*, 17: 23-31.
- 1200 Spring, K., S. Cross, C. Li, D. Watters, L. Ben-Senior, P. Waring, F. Ahangari, S. L. Lu, P. Chen, I.
1201 Misko, C. Paterson, G. Kay, N. I. Smorodinsky, Y. Shiloh, and M. F. Lavin. 2001. 'Atm knock-in
1202 mice harboring an in-frame deletion corresponding to the human ATM 7636del9 common
1203 mutation exhibit a variant phenotype', *Cancer Research*, 61: 4561-8.
- 1204 Staples, E. R., E. M. McDermott, A. Reiman, P. J. Byrd, S. Ritchie, A. M. Taylor, and E. G. Davies.
1205 2008. 'Immunodeficiency in ataxia telangiectasia is correlated strongly with the presence of two
1206 null mutations in the ataxia telangiectasia mutated gene', *Clinical and Experimental
1207 Immunology*, 153: 214-20.
- 1208 Stoyas, Colleen A, David D Bushart, Pawel M Switonski, Jacqueline M Ward, Akshay Alaghatta, Mi-bo
1209 Tang, Chenchen Niu, Mandheer Wadhwa, Haoran Huang, and Alex Savchenko. 2020.
1210 'Nicotinamide pathway-dependent Sirt1 activation restores calcium homeostasis to achieve
1211 neuroprotection in spinocerebellar ataxia type 7', *Neuron*, 105: 630-44. e9.
- 1212 Strich, Sabina J. 1966. 'Pathological findings in three cases of ataxia-telangiectasia', *Journal of
1213 Neurology, Neurosurgery, and Psychiatry*, 29: 489.
- 1214 Swift, M., D. Morrell, E. Cromartie, A. R. Chamberlin, M. H. Skolnick, and D. T. Bishop. 1986. 'The
1215 incidence and gene frequency of ataxia-telangiectasia in the United States', *American Journal of
1216 Human Genetics*, 39: 573-83.
- 1217 Sykora, Peter, Deborah L. Croteau, Vilhelm A. Bohr, and David M. Wilson, 3rd. 2011. 'Aprataxin
1218 localizes to mitochondria and preserves mitochondrial function', *Proceedings of the National
1219 Academy of Sciences of the United States of America*, 108: 7437-42.
- 1220 Takashima, H., C. F. Boerkoel, J. John, G. M. Saifi, M. A. Salih, D. Armstrong, Y. Mao, F. A. Quiocho,
1221 B. B. Roa, M. Nakagawa, D. W. Stockton, and J. R. Lupski. 2002. 'Mutation of TDP1, encoding
1222 a topoisomerase I-dependent DNA damage repair enzyme, in spinocerebellar ataxia with axonal
1223 neuropathy', *Nature Genetics*, 32: 267-72.
- 1224 Tal, Efrat, Marina Alfo, Shan Zha, Ari Barzilai, Chris I. De Zeeuw, Yael Ziv, and Yosef Shiloh. 2018.
1225 'Inactive Atm abrogates DSB repair in mouse cerebellum more than does Atm loss, without
1226 causing a neurological phenotype', *DNA Repair*, 72: 10-17.
- 1227 Tavani, F., R. A. Zimmerman, G. T. Berry, K. Sullivan, R. Gatti, and P. Bingham. 2003. 'Ataxia-
1228 telangiectasia: the pattern of cerebellar atrophy on MRI', *Neuroradiology*, 45: 315-19.
- 1229 Taylor, A. M., Z. Lam, J. I. Last, and P. J. Byrd. 2015. 'Ataxia telangiectasia: more variation at clinical
1230 and cellular levels', *Clinical Genetics*, 87: 199-208.
- 1231 Terplan, K. L., and R. F. Krauss. 1969. 'Histopathologic brain changes in association with ataxia-
1232 telangiectasia', *Neurology*, 19: 446-54.
- 1233 Tsutsumi, S., M. Yamazaki, T. Miyazaki, M. Watanabe, K. Sakimura, M. Kano, and K. Kitamura. 2015.
1234 'Structure-function relationships between aldolase C/zebrin II expression and complex spike
1235 synchrony in the cerebellum', *Journal of Neuroscience*, 35: 843-52.
- 1236 Tumbale, Percy, Matthew J Schellenberg, Geoffrey A Mueller, Emma Fairweather, Mandy Watson,
1237 Jessica N Little, Juno Krahn, Ian Waddell, Robert E London, and R Scott Williams. 2018.
1238 'Mechanism of APTX nicked DNA sensing and pleiotropic inactivation in neurodegenerative
1239 disease', *The EMBO Journal*, 37: e98875.

Perez et al. Resubmission

- 1240 Vacchio, Melanie S., Alexandru Olaru, Ferenc Livak, and Richard J. Hodes. 2007. 'ATM deficiency
1241 impairs thymocyte maturation because of defective resolution of T cell receptor α locus coding
1242 end breaks', *Proceedings of the National Academy of Sciences*, 104: 6323-28.
- 1243 Vail, Graham, Aifang Cheng, Yu Ray Han, Teng Zhao, Shengwang Du, Michael M. T. Loy, Karl Herrup,
1244 and Mark R. Plummer. 2016. 'ATM protein is located on presynaptic vesicles and its deficit
1245 leads to failures in synaptic plasticity', *Journal of Neurophysiology*, 116: 201-09.
- 1246 Valentin-Vega, Y. A., and M. B. Kastan. 2012. 'A new role for ATM: regulating mitochondrial function
1247 and mitophagy', *Autophagy*, 8: 840-1.
- 1248 van der Burgt, I, K H Chrzanowska, D Smeets, and C Weemaes. 1996. 'Nijmegen breakage syndrome',
1249 *Journal of Medical Genetics*, 33: 153-56.
- 1250 Verhagen, Mijke M.M., Jean-Jacques Martin, Marcel van Deuren, Chantal Ceuterick-de Groote, Corry
1251 M.R. Weemaes, Berry H.P.H. Kremer, Malcolm A.R. Taylor, Michèl A.A.P. Willemsen, and
1252 Martin Lammens. 2012. 'Neuropathology in classical and variant ataxia-telangiectasia',
1253 *Neuropathology*, 32: 234-44.
- 1254 Voogd, Jan, and Mitchell Glickstein. 1998. 'The anatomy of the cerebellum', *Trends in Neurosciences*,
1255 21: 370-75.
- 1256 Wakasugi, M., T. Sasaki, M. Matsumoto, M. Nagaoka, K. Inoue, M. Inobe, K. Horibata, K. Tanaka, and
1257 T. Matsunaga. 2014. 'Nucleotide excision repair-dependent DNA double-strand break formation
1258 and ATM signaling activation in mammalian quiescent cells', *Journal of Biological Chemistry*,
1259 289: 28730-7.
- 1260 Wallis, LI, PD Griffiths, SJ Ritchie, CAJ Romanowski, G Darwent, and ID Wilkinson. 2007. 'Proton
1261 spectroscopy and imaging at 3T in ataxia-telangiectasia', *American journal of neuroradiology*,
1262 28: 79-83.
- 1263 Walter, Joy T, Karina Alvina, Mary D Womack, Carolyn Chevez, and Kamran Khodakhah. 2006.
1264 'Decreases in the precision of Purkinje cell pacemaking cause cerebellar dysfunction and
1265 ataxia', *Nature Neuroscience*, 9: 389-97.
- 1266 Weyemi, Urbain, Christophe E. Redon, Towqir Aziz, Rohini Choudhuri, Daisuke Maeda, Palak R.
1267 Parekh, Michael Y. Bonner, Jack L. Arbiser, and William M. Bonner. 2015. 'NADPH oxidase 4 is
1268 a critical mediator in Ataxia telangiectasia disease', *Proceedings of the National Academy of
1269 Sciences*, 112: 2121-26.
- 1270 Xu, Y., and D. Baltimore. 1996. 'Dual roles of ATM in the cellular response to radiation and in cell
1271 growth control', *Genes and Development*, 10: 2401-10.
- 1272 Yamasaki, Miwako, Kouichi Hashimoto, and Masanobu Kano. 2006. 'Miniature Synaptic Events Elicited
1273 by Presynaptic Ca^{2+} Rise Are Selectively Suppressed by Cannabinoid Receptor Activation in
1274 Cerebellar Purkinje Cells', *The Journal of Neuroscience*, 26: 86-95.
- 1275 Zhou, Haibo, Zhanmin Lin, Kai Voges, Chiheng Ju, Zhenyu Gao, Laurens W. J. Bosman, Tom J. H.
1276 Ruigrok, Freek E. Hoebeek, Chris I. De Zeeuw, and Martijn Schonewille. 2014. 'Cerebellar
1277 modules operate at different frequencies', *Elife*, 3: e02536.
- 1278 Zhu, L., B. Scelfo, F. Tempia, B. Sacchetti, and P. Strata. 2006. 'Membrane excitability and fear
1279 conditioning in cerebellar Purkinje cell', *Neuroscience*, 140: 801-10.

1280

Perez et al. Resubmission

1281 8.0 Figure Legends

1282 **Figure 1. New A-T mouse models expressing clinically related PTCs. A)** The *Atm* gene locus was
1283 targeted by homologous recombination of a targeting vector containing a modified NorCOMM cassette
1284 in intron one and the corresponding A-T PTC mutation in exon 3 to create the targeted *Atm*^{R35X} and
1285 *Atm*^{Q35X} ES cell lines. Following germline transmission of these alleles in mice, the floxed NorCOMM
1286 cassette was removed by Cre excision *in vivo* to produce the final *Atm*^{R35X} and *Atm*^{Q35X} mouse lines. **B)**
1287 Genotyping of A-T mouse models. PCR agarose gel of mouse DNA shows 151 bp wildtype (+) allele
1288 band and 241 bp Cre-excised targeted allele band. **C)** ATM levels were examined using immunoblot
1289 analyses of the spleen due to its high expression density in this tissue. Exemplar blots illustrate a gene
1290 dose effect of ATM protein expression in samples harvested from wildtype (+), heterozygous (R35X/+,
1291 Q35X/+), and homozygous *Atm*^{R35X/R35X} (R35X) and *Atm*^{Q35X/Q35X} (Q35X) mice as indicated. **D)** Breeding
1292 scheme schematic for double mutant and control mice for this study. **E)** *Atm*^{R35X/R35X}; *Aptx*^{-/-} mice
1293 develop an ataxia that at late stages results in a severe loss of motor coordination and ability to
1294 ambulate (see **Videos 1-4**). Abbreviations for panel 1: **hβA**-human beta Actin promotor; **ΔTK1**-delta
1295 TK1, inactivated Thymidine Kinase 1; **T2A**-self-cleaving peptide sequence; **Neo**-Neomycin gene;
1296 **PGKpA**-Phosphoglycerate kinase poly A tail; **loxP**-recombination elements are show as a blue
1297 triangle; orientation of the Gateway **attB** recombination elements by an orange arrow; orientation of the
1298 genotyping **F** and **R** primers is shown by green and blue arrows respectively; and engineered PTC
1299 sites are shown in exon 3 by a red circle.

1300 **Figure 2. Health and survivability of single and double mutant mice. A) Left:** The line color and
1301 symbol for each genotype is denoted and is consistent across all figures (1-8). **Right:** *Atm*^{R35X/R35X};
1302 *Aptx*^{-/-} mice weighed significantly less than all control genotypes as indicated by the growth curves (±
1303 95% confidence interval; dotted lines). Growth curve (*Atm*^{R35X/R35X}; *Aptx*^{-/-} vs. controls): Male k = 0.024
1304 vs. 0.011-0.019, Y_{max} = 21.8 vs. 32.9-41.0 g, (n = 3 to 18); Female k = 0.030 vs. 0.017-0.022, Y_{max} =
1305 16.9 vs. 23.3-31.3, (n = 2 to 19). Sum of squares F-test run across all curves: Male F_(12, 364) = 30.5,
1306 ****p<0.0001, Female F_(12, 339) = 28.3, ****p<0.0001. **B)** ATM deficient mice, regardless of APTX

Perez et al. Resubmission

1307 expression, displayed significantly lower survivability with ~55% of mice deceased by P400. No
1308 statistical differences between ATM deficient mice were detected. Moreover, a single wildtype copy of
1309 the *Atm* gene was sufficient to prevent premature death (no statistical difference detected between
1310 *Atm*^{R35X/+}; *Aptx*^{-/-} and *Atm*^{+/+}; *Aptx*^{+/+} mice). Log-rank (Mantel-Cox) tests across all ($\chi^2_{(6, 217)} = 48.4$,
1311 **** $p < 0.0001$), just the ATM deficient ($\chi^2_{(2, 217)} = 1.06$, $p = 0.6$), and single comparisons to wildtype (see
1312 figure) were conducted. Total number of animals indicated in panel **C**. **C**) Pie charts illustrating that
1313 ATM deficient mice displayed a high prevalence of thymomas based on postmortem necropsies.
1314 “Other” probable causes of death included enlarged livers, and obstructed kidneys. “Missing” mice
1315 were presumed dead and cannibalized by cage mates, cause of death unknown. **Figure 2-figure**
1316 **supplement 1, Figure 2-source data**

1317 **Figure 2-figure supplement 1. Animal weight for each time point and genotype. A)** The average
1318 weights are plotted for each genotype at each of the indicated time points. Growth curves without
1319 experimental, 2-way ANOVA with age and genotype as factors. Male: $F_{(10, 226)} = 5.6$, $p < 0.0001$; Female:
1320 $F_{(10, 197)} = 7.3$, $p < 0.0001$. **B)** The survivability of each genotype of mice are plotted for male and female
1321 individually.

1322 **Figure 3. *Atm*^{R35X/R35X}; *Aptx*^{-/-} mice develop a progressive loss in motor coordination. A)**
1323 *Atm*^{R35X/R35X}; *Aptx*^{-/-} mice take a similar amount of time to descend a vertical pole at P45, 120, and 210,
1324 but significantly longer at P400. These overall results were found to be similar for both male (left, $n = 2$
1325 to 12) and female (right, $n = 4$ to 12) mice. **B)** Consistent with the vertical pole test, the gait of
1326 *Atm*^{R35X/R35X}; *Aptx*^{-/-} mice measured during ambulation on a Catwalk gait analysis system was
1327 significantly different to controls by P400, but not before P210. This includes the percent of time a
1328 mouse spends with 3 vs. 1, 2, or 4 paws on the ground and the speed and cadence during each run
1329 across the platform. The effects of the two null mutations were generally similar between males (left, n
1330 = 4 to 21) and females (right, $n = 3$ to 18). **C)** Behavioral data for male (blue) and female (pink)
1331 *Atm*^{R35X/R35X}; *Aptx*^{-/-} (dark purple, left) and *Atm*^{+/+}; *Aptx*^{+/+} (orange, right) mice are plotted at P30 (left 2
1332 columns) and 400 (right 2 columns). Left-right asymmetries of the horizontal bars indicate a difference

Perez et al. Resubmission

1333 in performance between genotypes for the behavioral test listed in a column on the far left. A significant
1334 difference in the time to right during the righting reflex at P8 was observed in both Male and Female
1335 mice (bottom). **A** and **B** were examined via two-way ANOVA with age and genotype as factors followed
1336 by *potshot* Tukey's multiple comparison tests between $Atm^{R35X/R35X}$; $Aptx^{-/-}$ and each of the control
1337 genotypes. Behavioral tests in **C** were examined using a non-parametric Kruskal Wallace followed by
1338 *postdocs* Dunn's multiple comparisons tests. Symbol/color key: $Atm^{+/+}$; $Aptx^{+/+}$ (purple circle), $Atm^{+/+}$;
1339 $Aptx^{-/-}$ (blue diamond), $Atm^{R35X/R35X}$; $Aptx^{+/+}$ (green triangle), $Atm^{R35X/R35X}$; $Aptx^{-/-}$ (orange square),
1340 $Atm^{R35X/+}$; $Aptx^{-/-}$ (red inverted triangle) **Figure 3-figure supplement 1, Figure 3-source data**

1341 **Figure 3-figure supplement 1. $Atm^{R35X/R35X}$; $Aptx^{-/-}$ mice develop progressive ataxia. A)**
1342 $Atm^{R35X/R35X}$; $Aptx^{-/-}$ mice develop an ataxia that at late stages results in a severe loss of coordination
1343 and ability to ambulate. **B)** Additional gait analyses measuring stride length and time of overlap of the
1344 hindlimbs. Examined via two-way ANOVA with age and genotype as factors followed by *potshot*
1345 Tukey's multiple comparison tests between $Atm^{R35X/R35X}$; $Aptx^{-/-}$ and each of the control genotypes. **C)**
1346 Behavioral deficits are seen only in $Atm^{R35X/R35X}$; $Aptx^{-/-}$ mice across all behavioral tests and sexes.
1347 Behavioral tests were examined using a non-parametric Kruskal Wallace followed by *posthoc* Dunn's
1348 multiple comparisons tests.

1349 **Figure 4. The biophysical properties of PNs are significantly perturbed in $Atm^{R35X/R35X}$; $Aptx^{-/-}$**
1350 **mice. A)** Schematic diagram of intracellular recording from a single Purkinje neuron (PN) in an acute
1351 cerebellar tissue slice preparation used to examine their biophysical properties. **B) Left:** Voltage clamp
1352 measurements of PN neuron membrane properties were made from a 1 s, -5 mV step pulse as
1353 illustrated. **Right:** The membrane input resistance (R_m), time constant (τ), and capacitance (C_m) were
1354 perturbed in $Atm^{R35X/R35X}$; $Aptx^{-/-}$ compared to $Atm^{+/+}$; $Aptx^{+/+}$ mice. **C)** Current clamp recordings of PN
1355 action potentials (AP) after 2 nA step pulses from a -70 mV holding potential. PN action potentials
1356 recorded from $Atm^{R35X/R35X}$; $Aptx^{-/-}$ fail to maintain constant firing and summary plots show that they
1357 have lower 1st AP amplitudes, firing threshold, and area under the curve. **D) Top:** Example mEPSC
1358 traces taken from a PN under voltage clamp at a -80 mV holding potential. **Bottom:** Median frequency

Perez et al. Resubmission

1359 and amplitude data, along with the overall probability distribution function are plotted for both $Atm^{+/+}$;
1360 $Aptx^{+/+}$ (n = 11) and $Atm^{R35X/R35X}$; $Aptx^{-/-}$ (n = 11) mice. The frequency, but not amplitude of PNs recorded
1361 in $Atm^{R35X/R35X}$; $Aptx^{-/-}$ mice was found to be perturbed. **E and F) Left:** Example traces of evoked
1362 EPSCs recorded from PNs as a result of a 2-pulse stimulation (50 ms interval) of either parallel (**E**) or
1363 climbing (**F**) axon fibers. Traces illustrate the first (A_1) and second (A_2) amplitude (normalized) and time
1364 course of first decay (blue fitted line) of each synaptic response. **Right:** Summary plots of the paired
1365 pulse ratio. While parallel fiber paired pulse facilitation was normal in $Atm^{R35X/R35X}$; $Aptx^{-/-}$ mice, climbing
1366 fiber paired pulse depression and halfwidth was significantly perturbed compared to $Atm^{+/+}$; $Aptx^{+/+}$
1367 mice. Data in **B** were compared using an ANOVA (Kruskal-Wallis) followed by Dunn's multiple
1368 comparisons test while data in **D to F** were compared via Welch's *t*-test. Symbol/color key: $Atm^{+/+}$;
1369 $Aptx^{+/+}$ (purple circle), $Atm^{R35X/R35X}$; $Aptx^{-/-}$ (orange square) **Figure 4-figure supplement 1**

1370 **Figure 4-figure supplement 1. Current vs. voltage responses significantly differ between $Atm^{+/+}$;**
1371 **$Aptx^{+/+}$ and $Atm^{R35X/R35X}$; $Aptx^{-/-}$ mice. A)** PN voltage responses to various current steps between -500
1372 and 2250 pA (250 pA steps) from a -70 mV holding current in $Atm^{+/+}$; $Aptx^{+/+}$ (top, purple) and
1373 $Atm^{R35X/R35X}$; $Aptx^{-/-}$ (bottom, orange) mice. **(B)** I-V curves calculated from either max deflection ($V_{m\ max}$)
1374 or steady state ($V_{m\ end}$) for $Atm^{+/+}$; $Aptx^{+/+}$ (purple) and $Atm^{R35X/R35X}$; $Aptx^{-/-}$ (orange) mice. **(C)** Various
1375 measurements of the voltage response to -500 pA step pulse (blue box in **B**) in $Atm^{+/+}$; $Aptx^{+/+}$ (purple)
1376 and $Atm^{R35X/R35X}$; $Aptx^{-/-}$ (orange) mice. Significance was tested using a non-parametric Mann Whitney
1377 test.

1378 **Figure 5. Cerebellar atrophy is associated with a progressive reduction in PN neural action**
1379 **potential firing frequency and PN dendritic length. A)** Schematic diagram of extracellular recording
1380 from a single Purkinje neuron (PN) in an acute cerebellar tissue slice preparation. Example
1381 electrophysiological traces for $Atm^{+/+}$; $Aptx^{+/+}$ (purple, top) and $Atm^{R35X/R35X}$; $Aptx^{-/-}$ (orange, bottom) PNs
1382 in the medial (vermis) area of the cerebellum. **(B)** $Atm^{R35X/R35X}$; $Aptx^{-/-}$ PN action potential firing frequency
1383 progressively decreased with age and was significantly slower in comparison to all control genotypes
1384 expressing at least one copy of the *Atm* or *Aptx* gene. [$Atm^{+/+}$; $Aptx^{+/+}$ (n=52 to 59), $Atm^{+/+}$; $Aptx^{-/-}$ (n =

Perez et al. Resubmission

1385 51 to 64), $Atm^{R35X/R35X}; Aptx^{+/+}$ (n = 39 to 52), $Atm^{R35X/R35X}; Aptx^{-/-}$ (n = 24 to 71), $Atm^{R35X/+}; Aptx^{-/-}$ (n =
1386 69)] **C)** Cartoon image of the brain highlighting the dorsal forebrain and cerebellar surface. 2-
1387 dimensional area estimates from dorsal images of the brain were used to determine the cerebellum to
1388 forebrain ratio allowing us to control for any differences in overall size of the brain. We found the
1389 cerebellum decreased in size over age in $Atm^{R35X/R35X}; Aptx^{-/-}$ (n = 5 to 10), but not control mice [$Atm^{+/+};$
1390 $Aptx^{+/+}$ (n = 4 to 20), $Atm^{+/+}; Aptx^{-/-}$ (n = 4 to 12), $Atm^{R35X/R35X}; Aptx^{+/+}$ (n = 6 to 16), $Atm^{R35X/+}; Aptx^{-/-}$ (n =
1391 6)]. **D)** Immunofluorescent images of $Atm^{+/+}; Aptx^{+/+}$ (top) and $Atm^{R35X/R35X}; Aptx^{-/-}$ (bottom) at P400
1392 (medial cerebellar lobule VIII). Scale bar = 50 μ m **E)** The width of the molecular layer, but not the
1393 granule cell layer progressively declined over age (n = 5 to 7). Statistical significances were assessed
1394 via 2-way ANOVA with age and genotype as factors followed by *posthoc* Holm-Sidak (**B, C, and E**
1395 **(top)**) or Sidak (**E bottom**) pairwise multiple comparisons test. **Figure 5-figure supplements 1-5,**
1396 **Figure 5-source data**

1397 **Figure 5-figure supplement 1. Mean PN firing frequency across the cerebellum.** Average PN firing
1398 frequency is plotted across the indicated locations at P45, 120, 210, and 400.

1399 **Figure 5-figure supplement 2. Mean PN firing frequency across genotype and sex.** Average PN
1400 firing frequency for all cells recorded from male and female mice is plotted for the indicated genotype.
1401 No significant differences were observed between sex. 2-Way ANOVA with age and sex as factors,
1402 $Atm^{+/+}; Aptx^{+/+}$ ($F_{(1, 751)} = 1.15, p=0.3$), $Atm^{+/+}; Aptx^{-/-}$ ($F_{(1, 797)} = 1.10, p=0.3$), $Atm^{R35X/R35X}; Aptx^{+/+}$ ($F_{(1, 630)} =$
1403 $0.17, p=0.7$), $Atm^{R35X/R35X}; Aptx^{-/-}$ ($F_{(1, 666)} = 1.10, p=0.4$), *t*-test for P400 $Atm^{R35X/+}; Aptx^{-/-}$ ($p=0.9$)

1404 **Figure 5-figure supplement 3. Coefficient of Variation of PN firing frequency across the**
1405 **cerebellum.** Average CV of PN firing frequency is plotted across the indicated locations at P45, 120,
1406 210, and 400. No significant differences ($p<0.5$) were detected across all areas using 2-way ANOVA
1407 with age and genotype as factors.

1408 **Figure 5-figure supplement 4. Mean variation between PN firing intervals across the cerebellum.**
1409 Average CV2 of PN firing frequency is plotted across the indicated locations at P45, 120, 210, and 400.

Perez et al. Resubmission

1410 No significant differences ($p < 0.5$) were detected across all areas using 2-way ANOVA with age and
1411 genotype as factors.

1412 **Figure 5-figure supplement 5. Histopathological effects of ATM and APTX deficiency. A)** Width
1413 measurements of the molecular and granule cell layer (ML and GCL respectively) for each folia across
1414 the medial intermediate and lateral areas of the cerebellum. **B) (Top)** Summary plot indicates no
1415 significant differences in the 2D linear density of PNs across each folia in $Atm^{R35X/R35X}; Aptx^{-/-}$ vs. $Atm^{+/+};$
1416 $Aptx^{+/+}$. **(Bottom)** Images of parasagittal cerebellar slices (2.5X) illustrating the lack of significant gaps
1417 in PN (green, Calbindin) or granule cell layers (magenta, DAPI). Scale bar = 0.5 mm **(C)** Images of
1418 parasagittal sections from $Atm^{+/+}; Aptx^{+/+}$ (top row) and $Atm^{R35X/R35X}; Aptx^{-/-}$ (bottom rows) mice (63X).
1419 PNs (green, Calbindin) were found to have a larger diameter than those found in $Atm^{+/+}; Aptx^{+/+}$ cells
1420 (red arrows). PN axonal swellings were also observed in $Atm^{R35X/R35X}; Aptx^{-/-}$ sections (magenta arrows).
1421 Scale bar = 50 μ m

1422 **Figure 6. T-cell deficits are found in the blood of $Atm^{R35X/R35X}; Aptx^{-/-}$ mice. A)** Representative flow
1423 cytometric profiles of T-cell glycoprotein marker CD3 and summary plots indicate ATM and/or APTX
1424 deficient mice have decreased proportions of CD3⁺ T-cells in the blood. **B)** Representative flow
1425 cytometric profiles of T-cell glycoprotein markers CD4 and CD8 gated on CD3⁺ cells and summary plots
1426 for CD8 and CD4 single positive cell proportions. ATM deficient mice had reduced CD4⁺ proportions
1427 compared to mice with at least one copy of the *Atm* gene. Statistical significances were assessed via 1-
1428 way ANOVA followed by *posthoc* Tukey's pairwise multiple comparisons tests. Number of animals
1429 denoted at bottom of bar. Symbol/color key: $Atm^{+/+}; Aptx^{+/+}$ (purple circle), $Atm^{R35X/R35X}; Aptx^{+/+}$ (green
1430 triangle), $Atm^{R35X/+}; Aptx^{-/-}$ (red inverted triangle), $Atm^{R35X/R35X}; Aptx^{-/-}$ (orange square) **Figure 6/7-source**
1431 **data**

1432 **Figure 7. ATM and APTX deficiency confer deficits in T-cell expression, but at different**
1433 **developmental stages. A)** Representative flow cytometric profiles of T-cell glycoprotein markers CD44
1434 and CD25 gated on CD4⁻CD8⁻ double negative (DN) cells. Summary plots show proportions of
1435 thymocytes at DN stages 1-4 (left to right). APTX deficient mice display increased proportions for DN1-

Perez et al. Resubmission

1436 3 and decreased proportion at DN4 consistent with a deficit in ontogeny from DN3 to DN4. **B)**
1437 Representative flow cytometric profiles of T-cell glycoprotein markers CD4 and CD8 gated. ATM
1438 deficient mice display decreased proportions for CD4 and CD8 single positive cells consistent with a
1439 deficit in ontogeny from CD4⁺CD8⁺ double positive to CD4⁺ and CD8⁺ single positive fates. Statistical
1440 significances were assessed via 1-way ANOVA followed by *posthoc* Tukey's pairwise multiple
1441 comparisons tests. Number of animals denoted at bottom of bars. Symbol/color key: *Atm*^{+/+}; *Aptx*^{+/+}
1442 (purple circle), *Atm*^{R35X/R35X}; *Aptx*^{+/+} (green triangle), *Atm*^{R35X/+}; *Aptx*^{-/-} (red inverted triangle), *Atm*^{R35X/R35X};
1443 *Aptx*^{-/-} (orange square)

1444 **Figure 8. ATM protein expression is restored after readthrough compound exposure in explant**
1445 **tissues from *Atm*^{R35X/R35X} and *Atm*^{Q35X/Q35X}.** Spleen and cerebellar explant tissue from *Atm*^{R35X/R35X} and
1446 *Atm*^{+/+} mice were treated with vehicle, the readthrough compounds G418 (100 μM), or GJ103 (100 μM)
1447 for 72 hrs. ATM immunoblots show recovery of ATM (MW 350 kDa) production in both the spleen (n = 2)
1448 and cerebellum (n = 3). Equal loading was assessed via housekeeping genes (Actin or GAPDH) and
1449 ponceau staining. **Figure 8-source data**

1450 11.0 Source files

1451 **Figure 2- source data. Weight, age of death, and probable cause of death**

1452 **Figure 3-source data. Raw behavior data**

1453 **Figure 4-source data. Electrophysiological data**

1454 **Figure 5- source data. Individual average firing frequencies for each recorded cell; Individual CV**
1455 **for each recorded cell; Brain area**

1456 **Figure 6/7- source data. Tables of FACs data**

1457 **Figure 8-source data. Western blot measurements**

1458 12.0 Rich Media

1459 **Video 1. Pole test, *Atm*^{+/+} vs. *Atm*^{R35X/R35X}.** *Atm*^{R35X/R35X} do not display an ataxic phenotype at P460.

1460 **Video 2. Pole test, *Aptx*^{+/+} vs. *Aptx*^{-/-}.** *Aptx*^{-/-} mice do not display an ataxic phenotype at P460.

1461 **Video 3. Pole test, *Atm*^{+/+}; *Aptx*^{+/+} vs. *Atm*^{R35X/R35X}; *Aptx*^{-/-}.** *Atm*^{R35X/R35X}; *Aptx*^{-/-} have considerable
1462 motor disability at P460.

1463 **Video 4. Open field, *Atm*^{+/+}; *Aptx*^{+/+} vs. *Atm*^{R35X/R35X}; *Aptx*^{-/-}.** *Atm*^{R35X/R35X}; *Aptx*^{-/-} display a clear
1464 inability to ambulate in the open field at P460.

Perez et al. Resubmission

1465

1466

1467

1468

Fig. 1

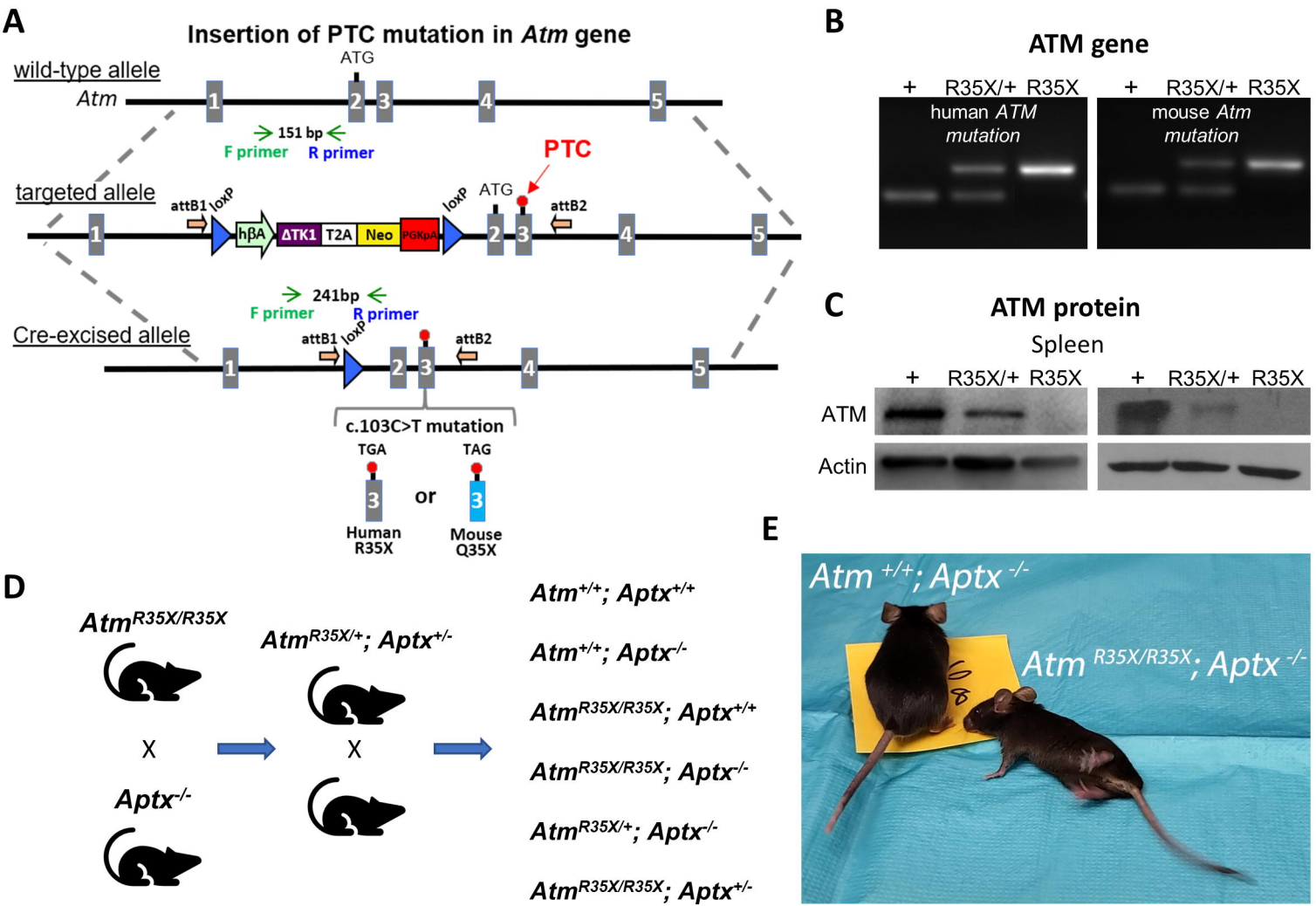
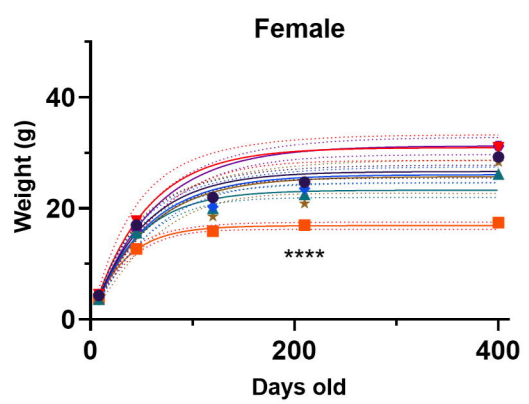
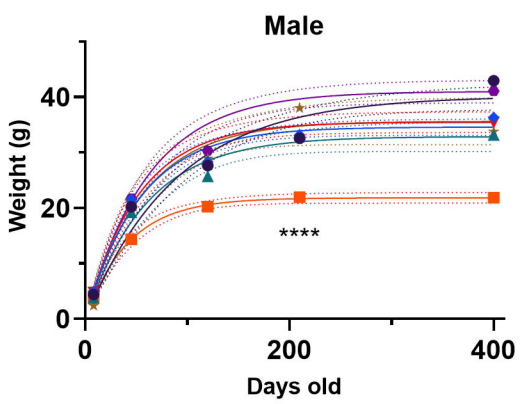


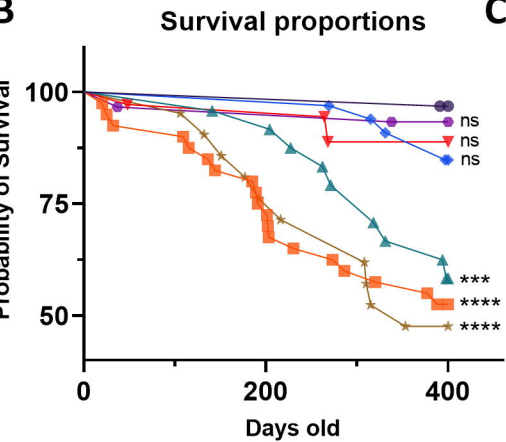
Fig. 2

A

- *Atm*^{+/+}; *Aptx*^{+/+}
- ◆ *Atm*^{+/+}; *Aptx*^{-/-}
- ▲ *Atm*^{R35X/R35X}; *Aptx*^{+/+}
- *Atm*^{R35X/R35X}; *Aptx*^{-/-}
- ▼ *Atm*^{R35X/+}; *Aptx*^{-/-}
- ★ *Atm*^{R35X/R35X}; *Aptx*^{+/-}
- *Atm*^{R35X/+}; *Aptx*^{+/+}



B



C

- Cause of death**
- thymoma
 - indeterminable
 - other
 - missing
 - alive at 400d

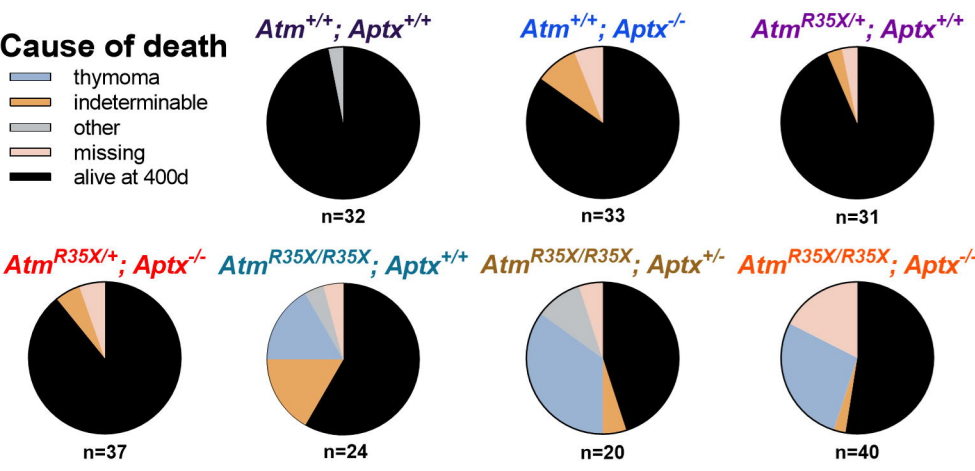


Fig. 3

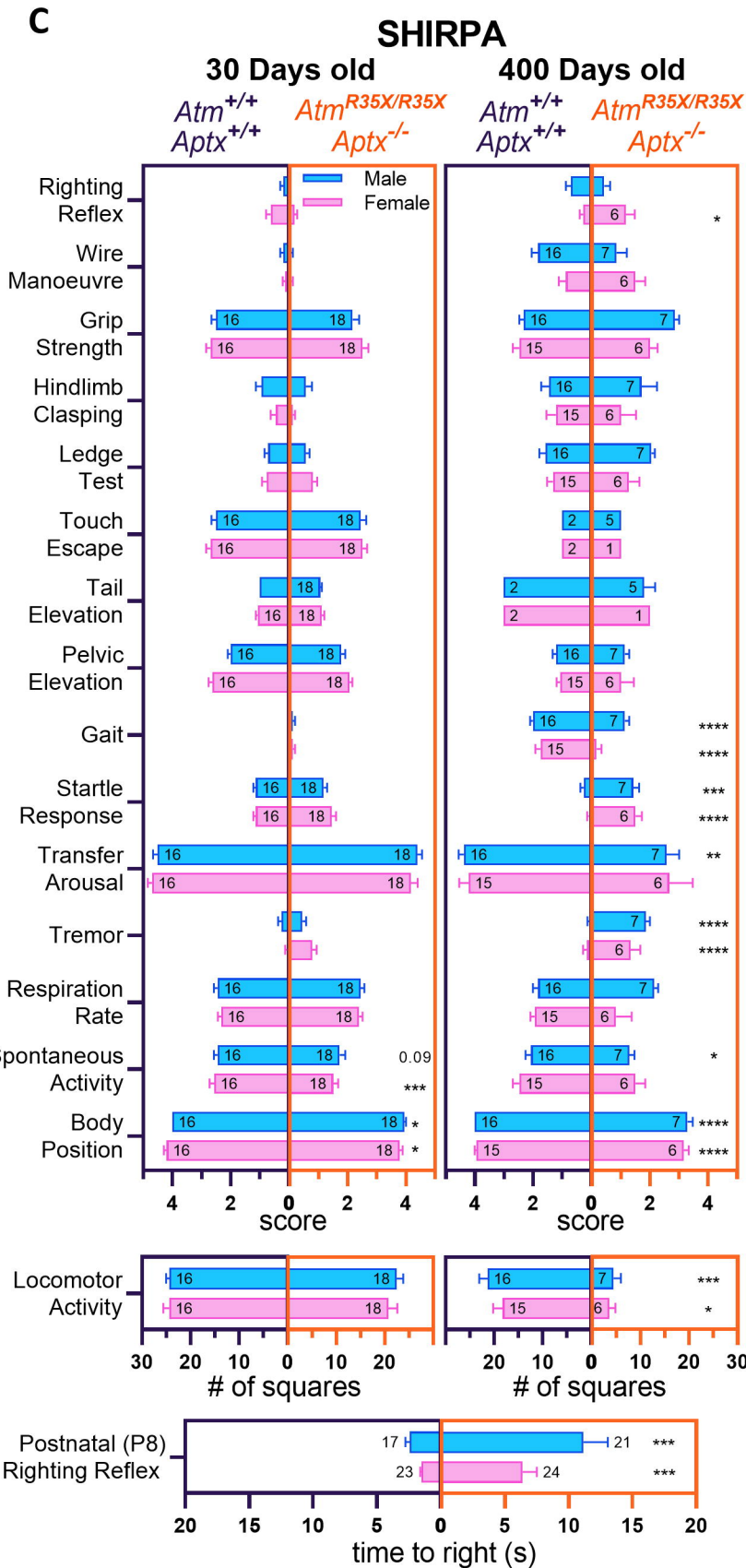
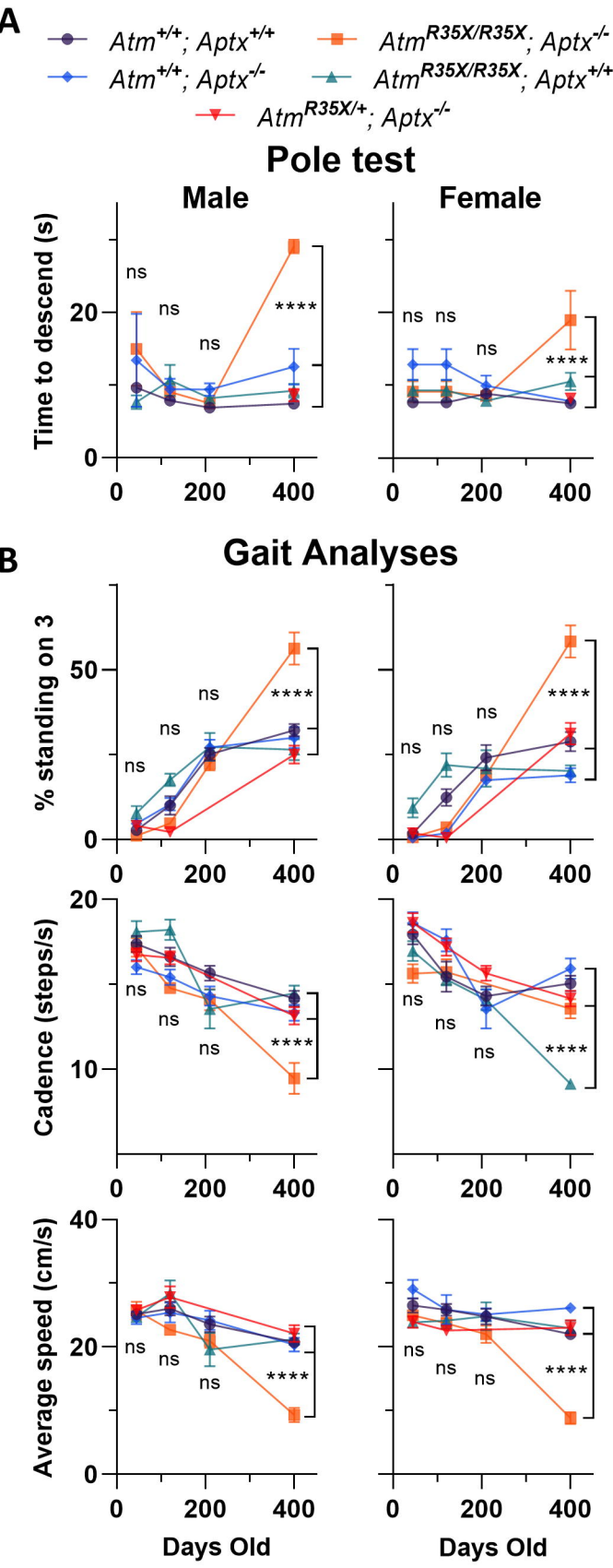


Fig. 4

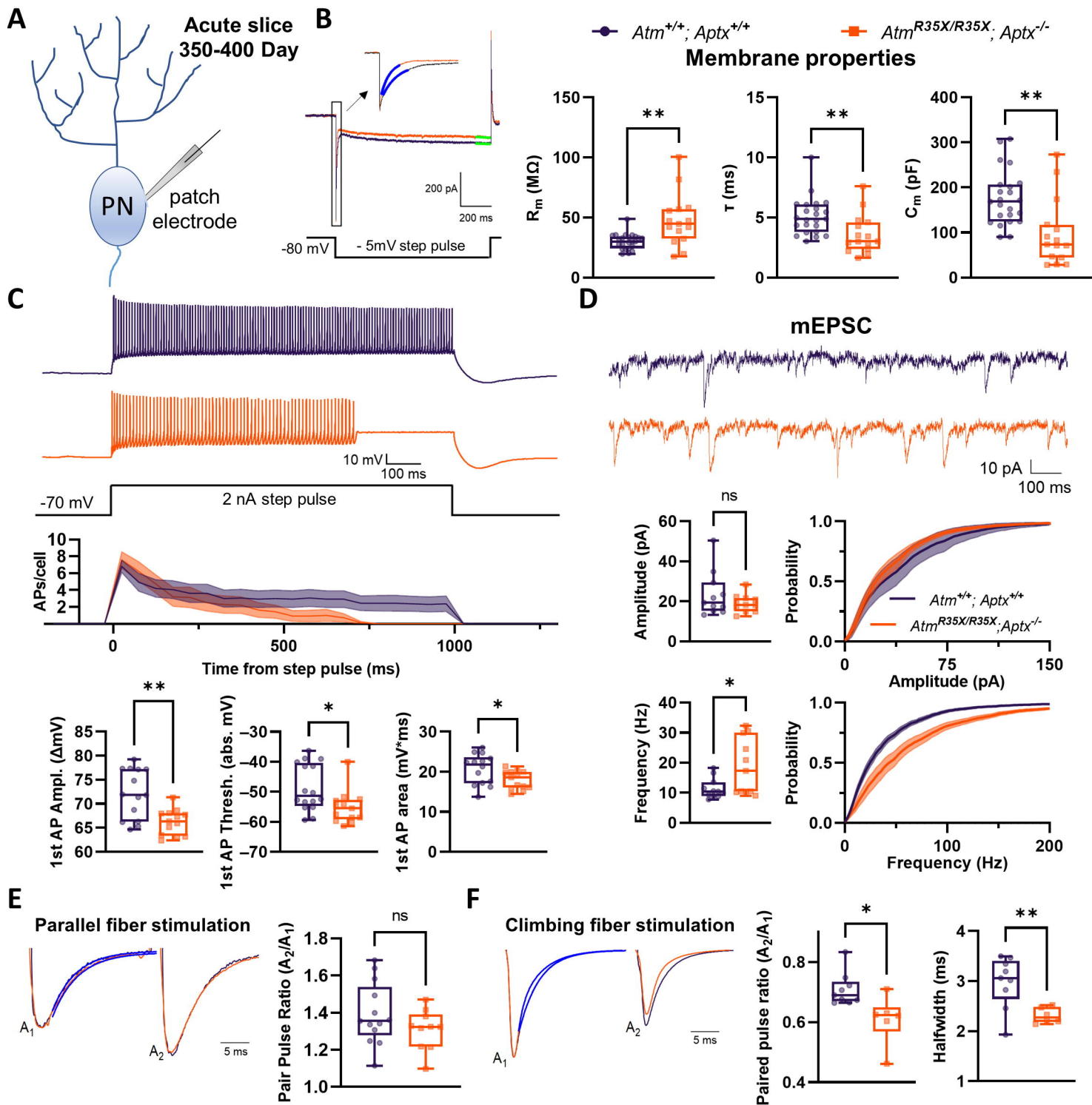


Fig. 5

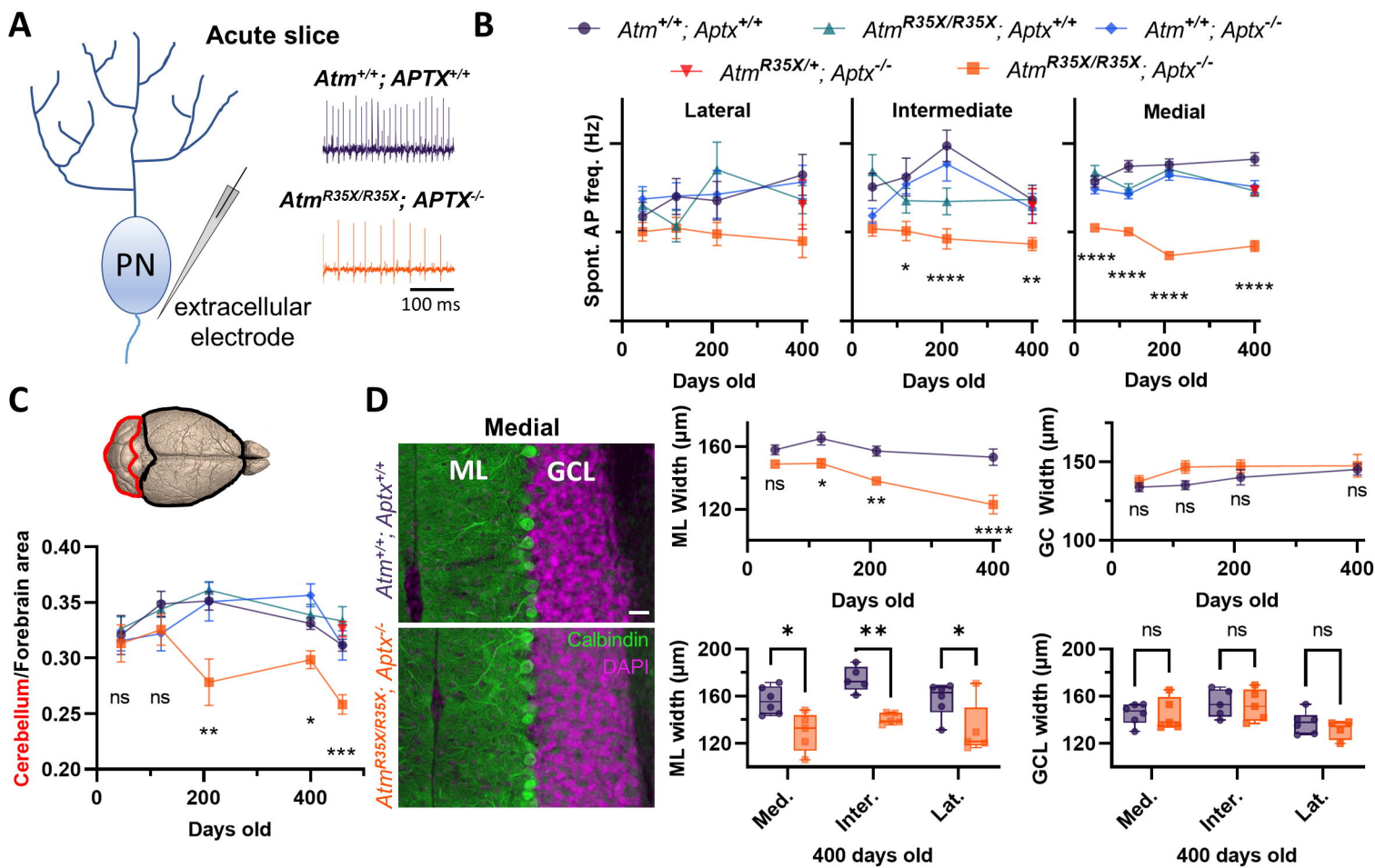


Fig. 6

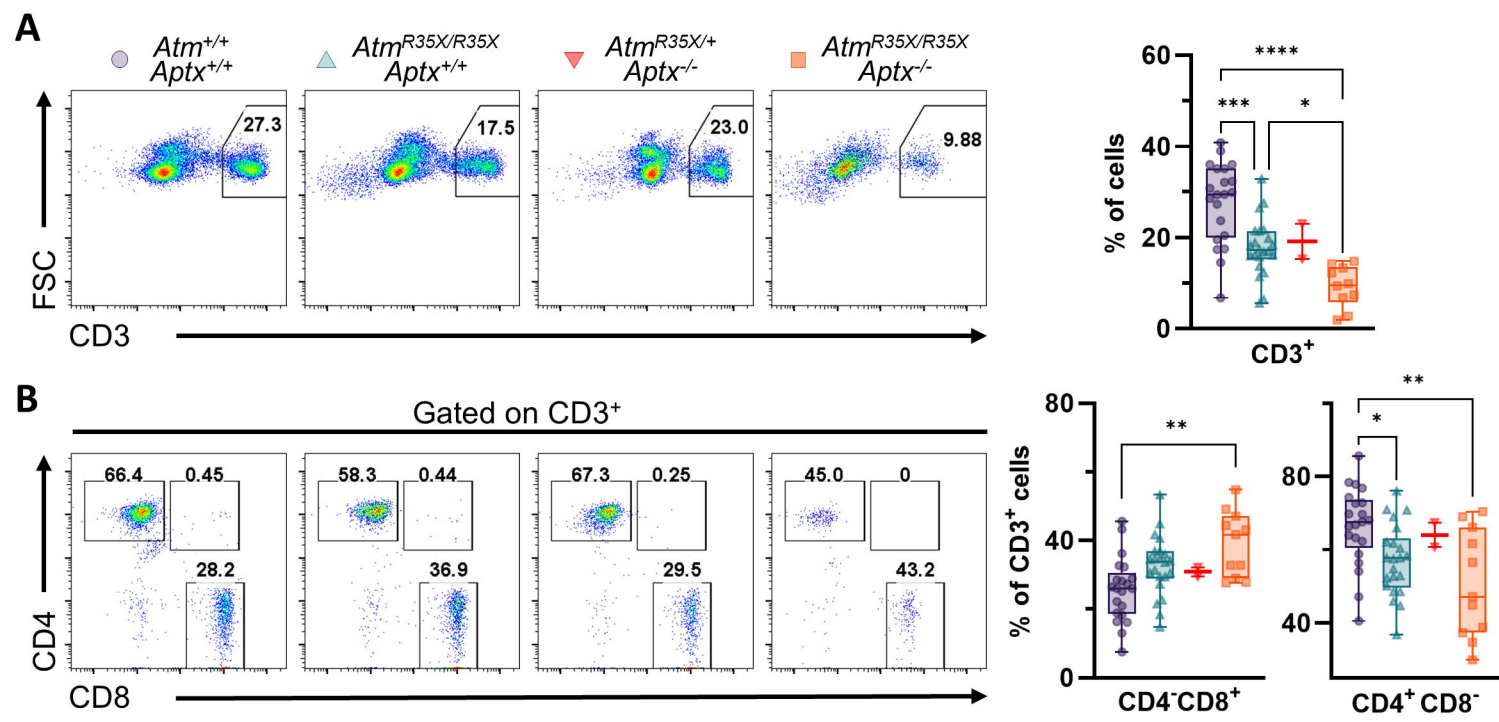


Fig. 7

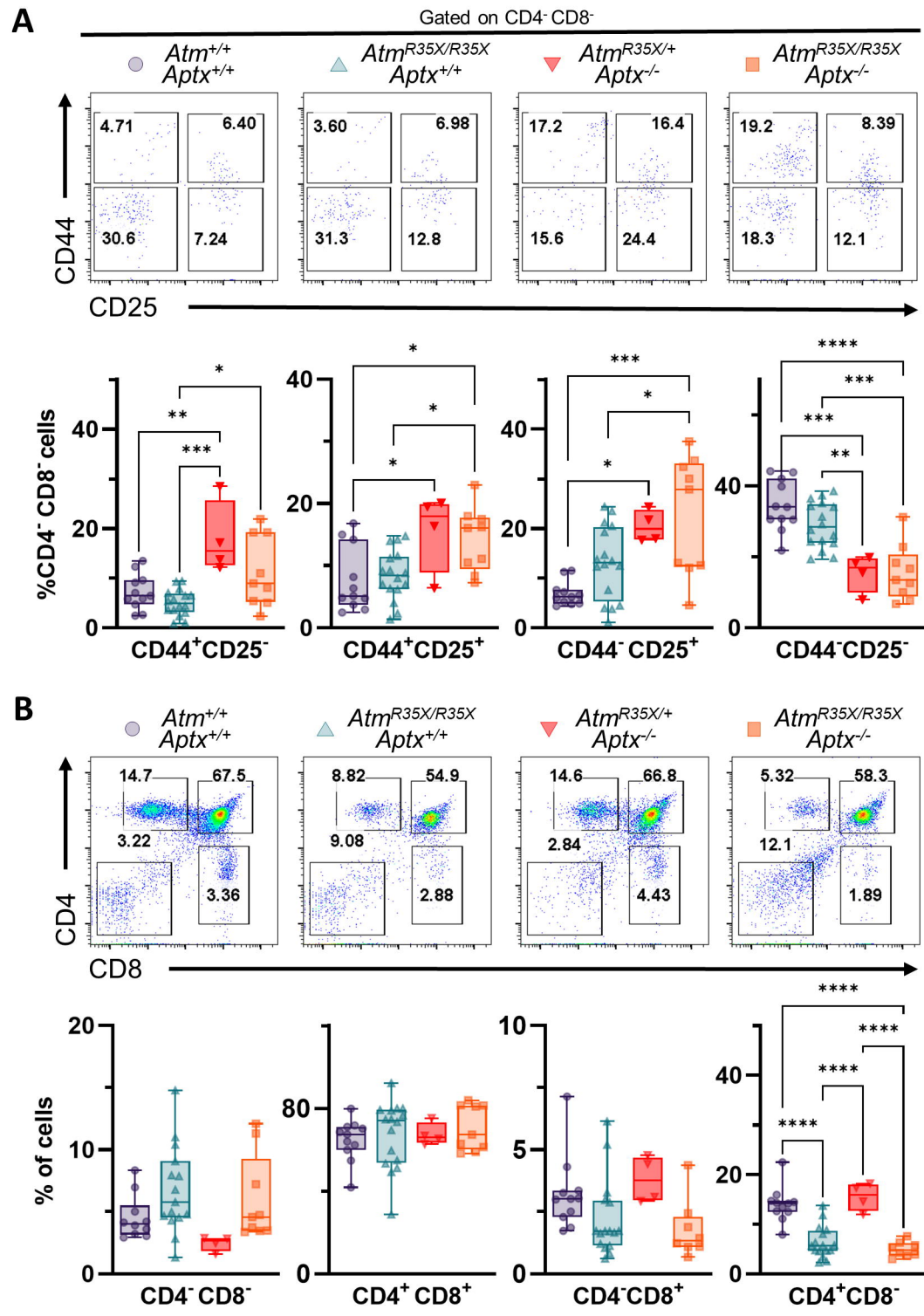


Fig. 8

